

UNIVERSITÀ DEGLI STUDI DI NAPOLI “FEDERICO II”

Dipartimento di Ingegneria Chimica, dei Materiali e
della Produzione Industriale



Dottorato di ricerca in Ingegneria Chimica

XXV CICLO

Deformation of surfactant vesicles in shear flow

Scientific committee

Prof. Stefano Guido

Ing. Sergio Caserta

Ing. Vincenzo Guida

Candidate

Angelo Pommella

Abstract

Vesicle dynamics is a multidisciplinary topic of growing scientific interest spanning from physics to engineering and biology. While most studies have been so far addressed to unilamellar phospholipid vesicles, which can be regarded as a model system of living cells, less attention has been devoted to multilamellar vesicles, which are an intriguing example of soft matter found in surfactant-based everyday life products, such as detergents, foodstuff, and cosmetics. In this work, we present the first quantitative investigation of the flow behaviour of single SMLVs. We found that SMLVs are deformed and oriented by the action of shear flow while keeping constant volume, and exhibit complex dynamic modes (i.e., tumbling, breathing and tank-treading). Moreover, SMLV deformation and orientation scale with radius R in analogy with emulsion droplets and elastic capsules (instead of R^3 such as in unilamellar vesicles).

However one of the key issues is how the packed, onion-like microstructure of SMLVs is capable of undergoing the large tank-treading deformations which are observed under simple shear. By rheo-optical experiments in a parallel-plate shear device, we show that tank-treading vesicle deformation is associated with a core-shell microstructure, where the former is a pool of an isotropic micellar phase and the latter is made of smectic lamellar layers. The outer shell is rearranged by convection with accumulation at the vesicle ends and thinning in the central part, where formation of typical liquid crystalline defects (focal conical domains) is found. These results are further

supported by the scaling analysis of vesicle retraction upon cessation of flow, which can be explained in terms of a dilational energy in the same way as the focal conical domain defects.

A possible application of the physical insight provided by this work is in the rationale design of processing methods of surfactant-based systems. These systems can be used in the pharmaceutical applications where different catalytic reactions are currently run in batch and homogenous conditions. In fact there are different studies aiming to run several catalytic reactions in continuous flow reactors and heterogeneous conditions in order to increase the efficiency of the process. One of these reactions is the Buchwald-Hartwig aryl amination that is run in batch and homogenous conditions in the industrial applications. In this work the Buchwald-Hartwig reaction is reported in a home-made continuous plug flow tube microreactor, using a homogeneous well-defined palladium-N-heterocyclic carbene [Pd(NHC)] complex. The microreactor enabled a 100% conversion of the reagents within 30 minutes, even at very low catalyst concentrations. A direct comparison between batch and continuous flow reactions is described and shows that the Buchwald-Hartwig reaction is faster in the microreactor than in the batch case. An investigation of the influence of the operating parameters of the microreactor on the reaction was carried out. Increasing temperature allowed a faster conversion of the reagents; moreover, no effect on microreactor performance was found by changing tube diameter. The dependence of reaction kinetics on reagents and [Pd(NHC)] pre-catalyst

concentrations was investigated based on initial reaction rates. The resulting expression for the rate of reaction showed some similarities with the one reported for palladium-phosphine catalyst, but also some important differences.

Table of contents

1. Introduction	1
1.1. Surfactant phase structures	2
1.1.1. Micellar phase	6
1.1.2. Lamellar phase	10
1.1.3. Vesicles	12
1.1.3.1. Unilamellar vesicles	13
1.1.3.2. Multilamellar vesicles	13
1.2. Buchwald-Hartwig reaction	14
1.3. Scope of the thesis	17
2. Theoretical background	18
2.1. Simple shear flow	18
2.1.1. Taylor theory	19
2.1.2. Cox theory	20
2.1.3. Retraction theory	22
2.2. Tube flow	22
2.2.1. Newtonian fluid	24
2.2.2. Non-newtonian fluid	25
2.2.3. Hetsroni theory	26

3. Experimental section	28
3.1. Materials	28
3.1.1. Multilamellar vesicles	28
3.1.2. Buchwald-Hartwig reaction	30
3.2. Methods	30
3.2.1. Rheology	30
3.2.2. Flow cell	30
3.2.3. Capillary flow	32
3.2.4. Image analysis	33
3.2.5. Confocal microscopy	37
3.2.6. Batch reactor	38
3.2.7. Continuous flow reactor	38
3.2.8. Analytical method	39
4. Results and discussions	41
4.1. Vesicle behaviour under simple shear flow	41
4.1.1. Rheological results	41
4.1.2. Dynamic behaviour	42
4.1.3. Internal structure	50
4.1.4. Start-up and retraction	60
4.2. Vesicle behaviour under capillary flow	64
4.3. Buchwald-Hartwig reaction	73

4.3.1. Batch experiments	74
4.3.2. Continuous flow experiments	76
5. Conclusions	85
6. Bibliography	88
7. Appendix	96
7.1. Publications	96
7.2. Conferences	97

1. Introduction

Nowadays the surfactant systems take on a great importance in the industrial processes; indeed they make up the basis of several commercial products such as house and personal care, foodstuff and pharmaceutical products. Moreover the surfactant systems raise a great interest in the scientific field because of their characteristic features that allow them to create complex structures. Surfactants have an amphoteric behaviour due to the presence of both a hydrophilic and hydrophobic group chemically linked inside their molecule; usually the hydrophobic group (i.e. tail) is made up by hydrocarbon chains that could be branch, linear or aromatic while the hydrophilic one (i.e. head) is formed by a polar group such as sulphate, phosphate or cetyl trimethylammonium bromide (CTAB). Their molecular structure lets the surfactants self-assembly creating different phase structures when they are dissolved in solvents like water for example. Moreover the rheological properties of these surfactant water-based systems are closely related to the presence of these structures; in fact a dramatically change in the rheology of surfactant systems can happen due to the change from a phase structure to another one. These changes are very interesting especially in the industrial processes because they could influence the design and setup of the industrial equipment.

In the next paragraphs an overview of the surfactant systems will be presented with a brief description of the most important phase structures (i.e. micellar and lamellar phase, multilamellar vesicles); consecutively an

introduction on the organic Buchwald-Hartwig (B-H) reaction will be presented. This reaction is currently run mainly in homogenous batch reactors with a great waste of the precious catalyst in the industrial applications. Consequently a great interest is recently grown towards B-H applications in continuous flow reactors working in heterogeneous systems in order to increase the productivity. The heterogeneous conditions can be obtained through the use of inorganic solvents together with the organic ones actually used; in this way great importance is acquired by surfactants and their phase structures in order to stabilize the reaction medium and improve the mass transfer between the two liquid phases. Moreover the use of different reaction conditions require new types of catalyst more efficient and stable than the ones actually used in the B-H reaction. Therefore in the following paragraphs a new type of catalyst is introduced and a description of continuous microfluidic devices is provided.

1.1. Surfactant phase structures

In water solutions ionic-surfactants tend to form aggregates from the micelles to the more complex series of mesomorph phases, referred to as liquid crystalline phases, depending on several parameters such as surfactant concentration and temperature. In Figure 1 some of the phase structures (a) present in a phase diagram (b) of a surfactant-water system are shown.

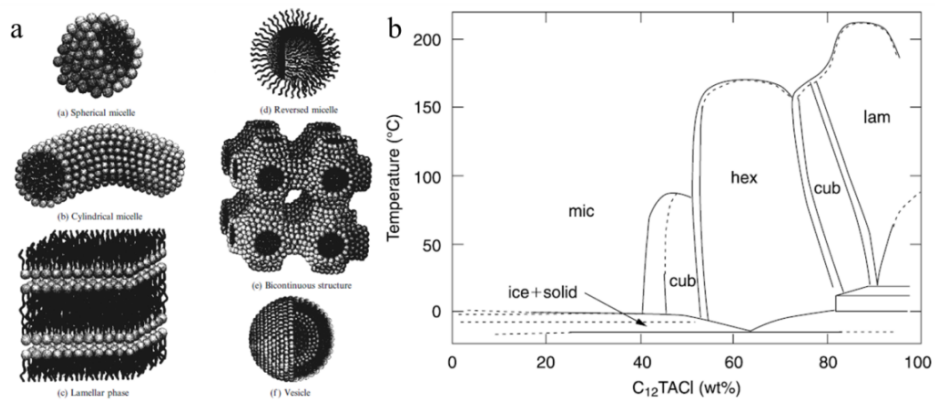


Figure 1. Phase structures¹ (a) and phase diagram² (b) of a surfactant – water system.

It can be seen in Figure 1b the strong influence of the temperature and the surfactant concentration on the existence of the different equilibrium phases.²

The presence of a particular phase structure in some conditions of the system is due to the competition between two opposite effects as shown in Figure 2; the heads solvation leads the surfactant molecule to separate themselves because of the repulsion among the hydrophilic heads while the attraction among the hydrophobic tails drives the aggregation of the surfactant molecules.

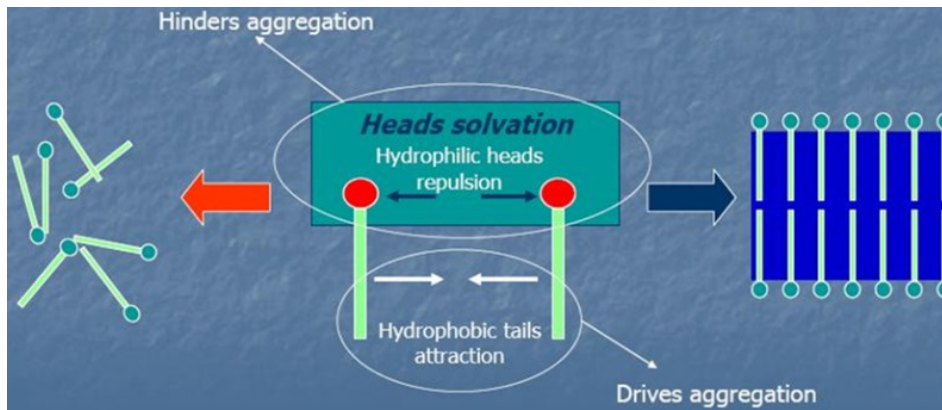


Figure 2. Picture of the principal forces governing the surfactant aggregation.

At very low surfactant concentration the repulsion forces prevail on the attraction ones and the molecules stay isolated in water; when the concentration is increased different aggregates, such as the micelles, start appearing because the attraction forces become more important. At high surfactant concentration more complex phase structures are present and the attraction forces prevail on the repulsion ones.³

A way to predict the presence of a specific phase structure at given conditions is the evaluation of the following dimensionless numbers:⁴

Packing parameter ($P = \frac{v}{a_0 l_c}$) based on the packing properties of the surfactant molecules where v is the volume of the hydrocarbon chain, a_0 is the head-group area and l_c is the maximum effective length that the chain can assume;

Hydrophilic-lipophilic balance ($HLB = 20 \frac{M_h}{M}$) where M_h is the molecular mass of the hydrophilic portion of the molecule and M is the molecular mass of the entire molecule.

In the surfactant water-based systems the packing parameter is usually preferred to the hydrophilic-lipophilic balance that is traditionally used to designate amphiphiles that form oil-in-water (O/W) or water-in-oil (W/O) micelles; however there is a linear proportionality between P and HLB.⁵

In Figure 3 the influence of several parameters (temperature, PH, molecular structure) is reported for the evaluation of the P and HLB number and consequently of the forces between the head-groups and the chains.

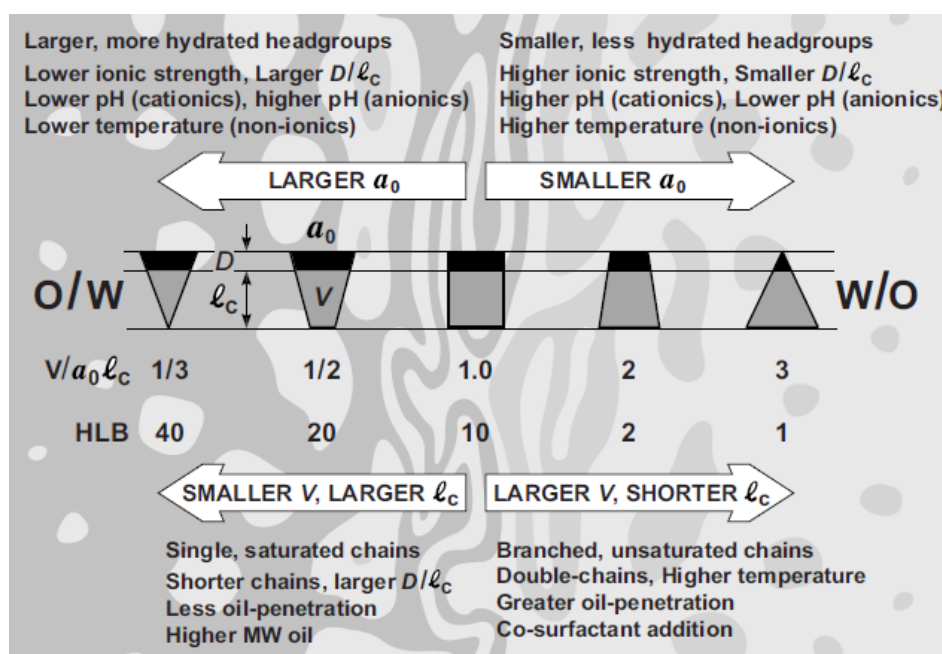


Figure 3. Influence of different parameters on the P and HLB number.⁴

In Figure 3 it's visible how the external conditions of the system (temperature, PH) can change the interactions among the surfactant molecules. This influence cause the presence of specific phase structures in the surfactant water-based systems; in fact in Figure 4 it's shown the

equilibrium phase structures present at different values of the P and HLB number.

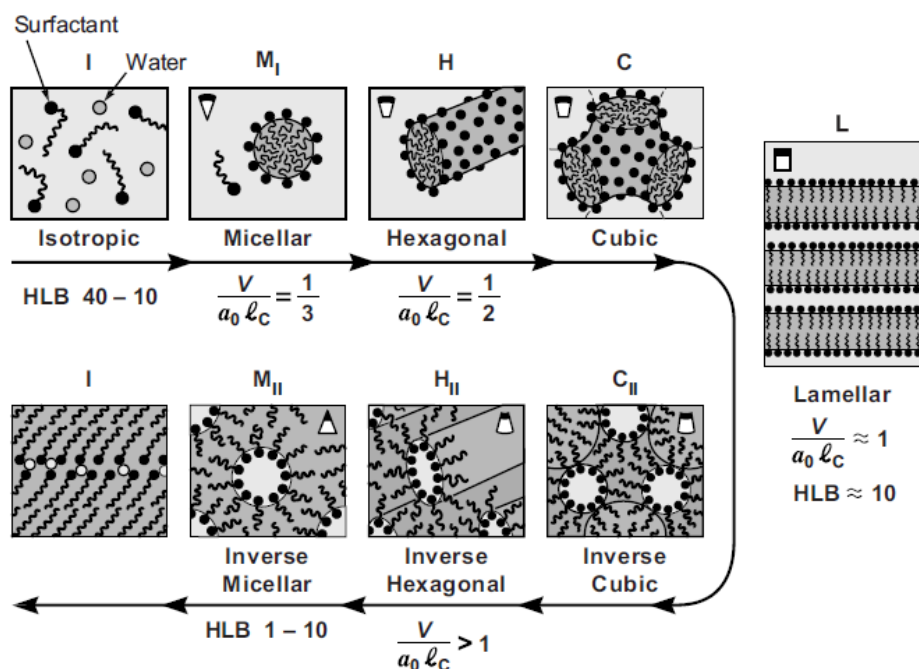


Figure 4. Several phase structures at different P and HLB number.⁴

Figure 4 shows the gradation in preferred structures with increasing P from micelles ($1/3 < P < 1/2$) to various interconnected structures to vesicles ($1/2 < P < 1$) and extended bilayers ($P \approx 1$) and finally to a family of “inverted” structures ($P > 1$) that are more common in presence of non-polar solvents.⁴

We shall now consider the more important structures in turn.

1.1.1. Micellar phase

The micellar or L_1 phase is characterized by the presence of aggregates (micelles) without any order about their orientation and position in solution; this phase shows the simplest kind of aggregates and it's usually found at low surfactant concentration in the phase diagrams. Every surfactant has a

minimum concentration below which the micelles don't exist and the surfactant molecules stay isolated in the solvent without self-aggregating; this concentration is called Critical Micelle Concentration (CMC) and its value depends on several parameters such as the surfactant molecule and the temperature.^{4,6}

As shown in Figure 5 the micelles can be spherical (top) or cylindrical (bottom) depending on the surfactant molecular structure and the solvent ionic strength especially.

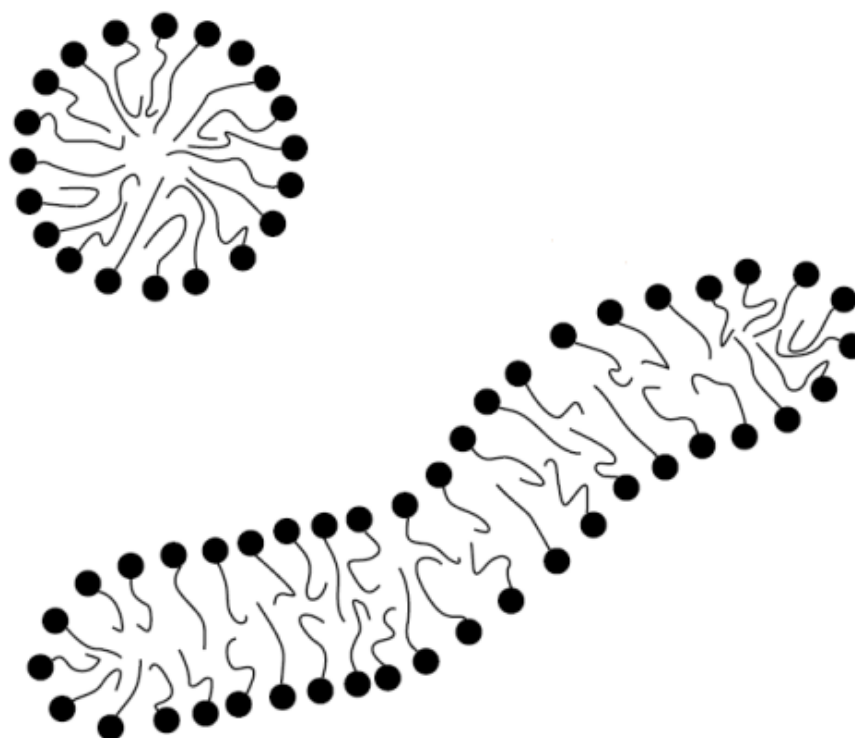


Figure 5. Spherical and cylindrical micelles.²

In order to know which kind of micelles are present in a surfactant solution, an evaluation of the dimensionless number P can be made:

$P \leq 1/3$ spherical micelles;

$1/3 \leq P \leq 1/2$ cylindrical micelles.

However, regarding the geometrical point of view, the generation of spherical micelles is possible until their radius is longer than surfactant tails otherwise cylindrical micelles will be present in the solution.⁶

The presence of spherical or cylindrical micelles influences the rheological behaviour of the surfactant systems. Indeed solutions with spherical micelles are usually newtonian with a viscosity slightly higher than the solvent one as well as in the case of suspensions of rigid spheres where the Einstein theory is valid³ (Figure 6).

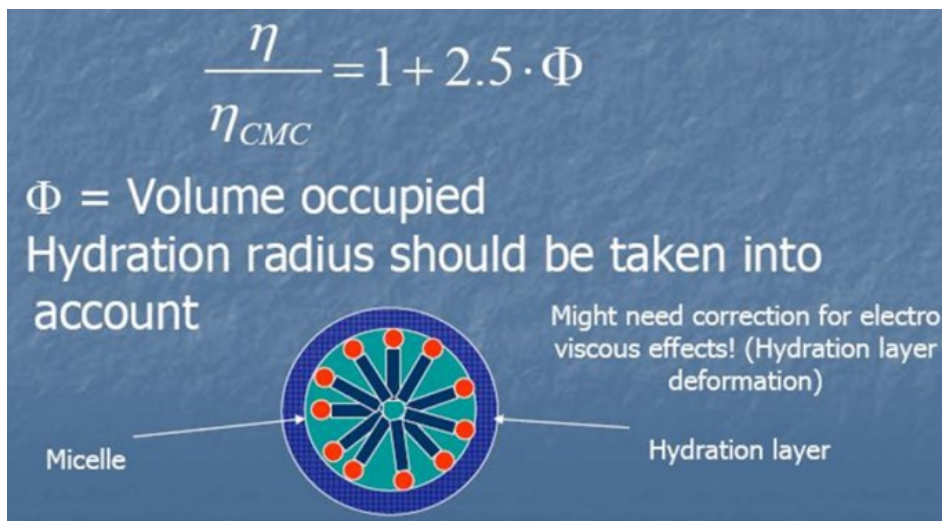


Figure 6. Influence of the hydration effect on the viscosity.

The difference shown in Figure 6 is that for spherical micelles the hydration effects must be considered for the evaluation of the viscosity while these effects are neglected in the case of the suspensions.

On the other hand the presence of cylindrical or worm-like micelles cause a viscoelastic behaviour in the rheological properties of the surfactant

solutions as well as in the polymeric systems. This behaviour is shown when the surfactant concentration is high enough to let the micelles overlap generating entanglements among them.² In Figure 7 the interactions among the cylindrical micelles are shown varying the surfactant concentration.

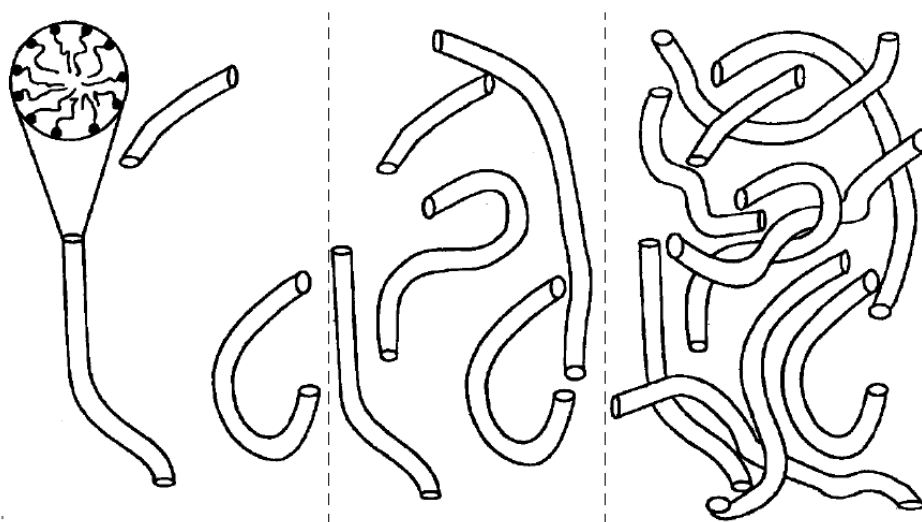


Figure 7. Interactions among the cylindrical micelles.²

This situation is similar to that observed with polymer solutions, and the viscosity of worm-like micelles can be analysed in terms of the motion of micelles using the reptation model of polymer systems. In this case, the micelles creep like a “snake” through tubes in a porous structure given by the other micelles.² A typical viscosity (left) with the elastic and viscous moduli (right) of surfactant systems showing cylindrical micelles⁷ are shown in Figure 8.

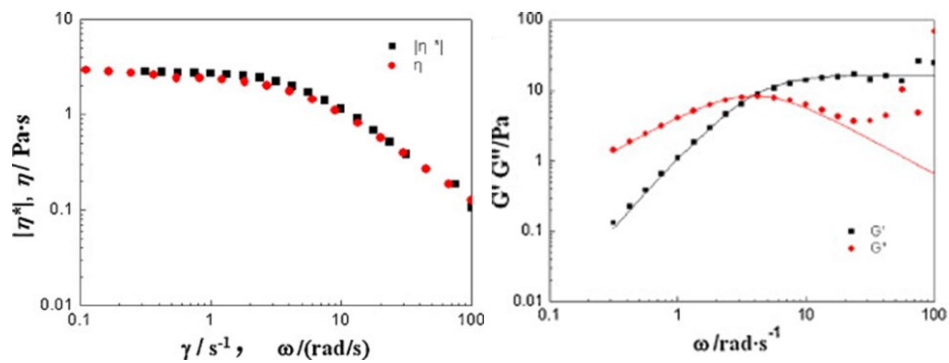


Figure 8. Rheology of the micellar phase.⁷

Despite of the similarity the polymers and the cylindrical micelles have a significant difference; in fact the polymers have a fixed length distribution of their chains due to their chemistry while the micelles can change their length breaking and recombining themselves under different conditions; this is the reason the worm-like micelles are called living polymers too.

1.1.2. Lamellar phase

The lamellar or L_{α} phase shows a sort of order about the orientation of the surfactant aggregates and is considered a liquid crystal phase. This phase is built of bilayers of surfactant molecules alternating with water layers as shown in Figure 9.

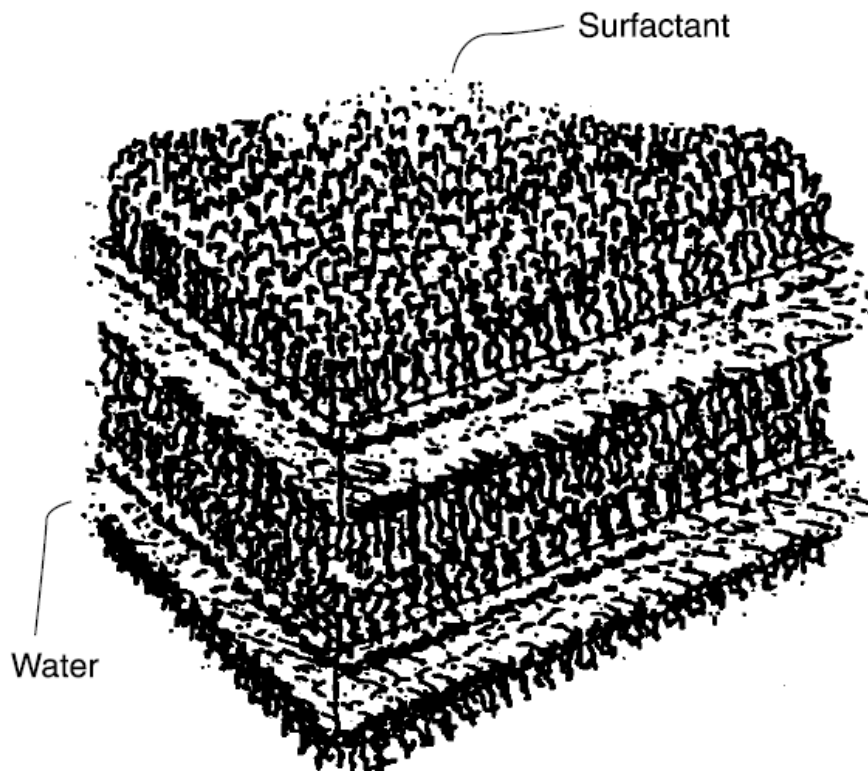


Figure 9. Surfactant bilayers.²

The thickness of the bilayers is somewhat lower than twice the surfactant molecule length. The thickness of the water layer can vary over wide ranges, depending on the nature and the concentration of the surfactant.² The surfactant bilayer can range from being stiff and planar to very flexible and undulating. Lamellar phases often extend down to $\approx 50\%$ surfactant. Below this, the stable phase changes to an isotropic micellar solution or other equilibrium phases.¹

Regarding the rheology, the lamellar phase shows a viscoelastic behaviour with a shear-thinning viscosity. Moreover there is a deep influence between the lamellar phase materials and the flow-history they are subjected; indeed

it's known the flow can induce a strong alignment of the lamellae making disappear some defects that could be present in this phase.⁸

1.1.3. Vesicles

Although extended planar bilayers are a thermodynamically favourable option for the association of some surfactants in aqueous solution, under certain conditions it is more favourable to form closed bilayer systems, leading to the existence of membranes and vesicles.⁴ Such a situation arises from two basic causes:

- (1) even large, highly extended planar bilayers possess edges along which the hydrocarbon core of the structure must be exposed to an aqueous environment, resulting in an unfavourable energetic situation;
- (2) the formation of an infinitely extended structure is unfavourable from an entropic standpoint.

The formation of spherical closed vesicles, then, addresses both those factors: the edge effect is removed by the formation of a closed system, and the formation of structures of finite size overcomes much of the entropic barrier. As long as the curvature of the vesicle is gentle enough to allow the packed molecules to maintain close to their optimum surface area, vesicles will represent viable structures for the association of surfactants and related materials.⁴

1.1.3.1. Unilamellar vesicles

Most of the literature concerns unilamellar vesicles⁹⁻¹¹ and it is commonly accepted that their deformation can be treated starting from Helfrich theory of elasticity of amphiphilic membranes,¹² which assumes a zero microscopic surface tension and quadratic curvature elasticity. A further assumption is that unilamellar vesicle volume is constant during deformation, based on the fact that, being bilayers only selectively permeable, a change in vesicle volume would result in a significant osmotic energy increase. A constant volume deformation requires a change in surface area, which could be generated by new amphiphiles joining the bilayer, or by the presence of an excess area, due to an "almost spherical" vesicle shape at rest. While the latter hypothesis has been tested experimentally on unilamellar vesicles,¹³ to our knowledge no similar study exists for surfactant multilamellar vesicles (SMLVs).

1.1.3.2. Multilamellar vesicles

Since their first appearance in the 1990s^{14, 15} the interest towards multilamellar vesicles has been continuously growing and several systems¹⁶⁻¹⁸ were studied in order to generate different kinds of vesicles¹⁹ for several applications. Examples are found both in the biomedical field, such as bio-membrane models²⁰ or carriers for drug delivery^{21, 22} and in industrial processing, such as phase transfer agents in multiphase chemical reactions.²³⁻²⁵ So far, most experimental studies were focused on the collective behaviour of multilamellar vesicles with the aim of finding

scaling relations between their size and an external flow field by several rheo-optical techniques, including small-angle light scattering, nuclear magnetic resonance (NMR), small-angle neutron scattering, and polarized light microscopy. By equating the shear stress to the elastic stress stored in a vesicle, in analogy with the classical work of Taylor on emulsion droplets,²⁶ it was found that the average size of surfactant multilamellar vesicles (SMLVs) is inversely dependent on the applied shear rate.²⁷⁻²⁹ On the other hand, only a few studies were addressed to the rheological behaviour of a single SMLV. From the theoretical point of view, an (effective) SMLV surface tension σ_{eff} ^{30,31} was derived based on the small deformation theory in analogy with sheared emulsion droplets or elastic capsules.³² It should be pointed out that unilamellar vesicles have zero interfacial tension and their rheological behaviour can be well described in terms of a bending modulus only.

1.2. Buchwald-Hartwig reaction

In the last decade, continuous flow operation has become a popular route for chemical synthesis, not only for large-scale production, such as in the petrochemical industry, but also for fine chemicals, such as in the pharmaceutical sector. As notable advantages, continuous-flow processes allow for a better control of selectivity and a more efficient handling of safety issues.³³⁻³⁵ The recent advancement in flow chemistry is also due to the optimization and adaptation of known reactions, by using microfluidics.³⁶ In particular, microreactors exhibit a large number of

advantages compared to traditional batch reactors.³⁷ We can cite as examples the significant enhancement of transport phenomena such as heat transfer and mixing processes,³⁸ the safety of operations, the precise control over residence time, the high surface-to-volume ratio,³⁶ the possibility of automation and the ease of scale-up operating several devices in parallel.³⁹ At present, for many pharmaceutical industries, where cost and time inefficient batch-based systems are employed, continuous flow microreactors are becoming of increasing interest. This reactor-type method has mostly been developed for cross-coupling reactions³⁹ that are widely used for the preparation of new drugs and materials.⁴⁰⁻⁴²

Cross-coupling products, such as arylamines, arylothers and diaryl ethers have reached great commercial importance in the pharmaceutical and in other industries, facilitating the construction of building blocks for supramolecular chemistry, organic materials and polymers. Among the plethora of cross-coupling reactions, the Buchwald-Hartwig (B-H) aryl amination reaction⁴³⁻⁴⁹ is one of the most efficient methodologies to prepare arylamines. This transformation involves the coupling of an aryl halide and a primary or secondary amine, using palladium as the metal catalyst and a relatively strong base (generally an alkoxide salt). One of the accepted reaction mechanism follows three steps: i) oxidative addition of the aryl halide to the palladium complex, ii) amine association/deprotonation on the palladium centre, releasing a halide salt and iii) reductive elimination, producing the desired arylamine and regenerating the palladium active

catalyst.⁵⁰ The rate equation for the described mechanism is provided in equation (1):⁵⁰

$$\frac{-d[ArBr]}{dt} = \frac{k_1 k_2}{k_{-1}[L]} [ArBr][Pd] \quad (1)$$

$[ArBr]$, $[L]$ and $[Pd]$ are respectively the aryl bromide, ligand and palladium concentrations and k_1 , k_2 and k_{-1} are the kinetic rate constants. Equation (1) has been developed for BINAP-ligated palladium complexes, where BINAP is a bidentate phosphine ligand, and assumes that the oxidative addition is the limiting step of the reaction. This rate equation shows that the reaction has direct linear first-order dependence on the aryl halide and palladium concentrations, an inverse first-order dependence on the ligand concentration and a zero-order dependence on the amine concentration.

The choice of operational conditions (substrate, catalyst, base, solvent, temperature)⁵¹ has an influence on the reaction kinetics and the optimization of the process.⁵² The choice of the palladium catalyst is also of crucial importance when performing the reaction. In the last decade, palladium-NHC complexes (NHC = N-heterocyclic carbene) have been developed as an alternative to the more classical palladium-phosphine systems, notably because NHC salts are easy to handle and air-stable in comparison with the sometimes air-sensitive phosphines. Moreover, these $[Pd(NHC)]$ complexes have proven to display a large number of advantages in cross-coupling reactions,⁵³⁻⁵⁹ allowing the reactivity of deactivated substrates under mild conditions, at low catalyst loadings, at room temperature, etc... More

specifically, we recently described [Pd(IPr*)(cin)Cl] (**1**) (IPr* = 1,3-bis(2,6-bis(diphenylmethyl)-4-methylphenyl)imidazol-2-ylidene) ; cin = cinnamyl, phenylallyl) as a very efficient pre-catalyst (pre-catalyst = before activation) for cross-coupling reactions,⁶⁰ especially for the Buchwald-Hartwig aryl amination reaction.⁶¹ Despite the high utility and efficiency of these palladium-NHC complexes, there are only few examples of their use in continuous flow reactors in the literature.⁶²⁻⁶⁵

1.3. Scope of the thesis

In this work of thesis the dynamic behaviour of the SMLVs of a commercial surfactant will be investigated. It will be observed how they behave, if they deform or not under shear flow. Their possible deformation will be analysed by using the well-known theory of the emulsion droplets and then analogies and differences between SMLVs and droplets will be investigated. In order to understand the mechanism governing the SMLV dynamics, their internal microstructure will be investigated at rest and under flow by using different microscopy techniques. Afterwards a further study will be carry out on the dynamic behaviour of SMLVs under capillary flow and the comparison with emulsion droplet behaviour will be shown.

Moreover a study on a new catalyst of the Buchwald-Hartwig reaction will be carry out in a microreactor and its performance will be compared with a batch reactor. A further preliminary study on the kinetics will be carry out on the new catalyst. Finally a change of the reaction conditions and the operative parameters will be investigated.

2. Theoretical background

In this chapter different theoretical models, developed for the emulsion droplets, are shown. These models were developed in different flow conditions (simple shear flow and tube flow) and will be used to analyse the deformation of the surfactant multilamellar vesicles in order to find analogies and differences between multilamellar vesicles and droplets.

2.1. Simple shear flow

The simple shear flow is a type of laminar flow that is generated by moving at a constant velocity v_p one of two parallel horizontal planes (see Figure 10). The shear flow is characterized by the shear rate $\dot{\gamma}$ defined as follows:

$$\dot{\gamma} = \frac{v_p}{\delta}$$

where δ is the gap between the two plates.

In Figure 10 the x direction represents the flow direction, the y direction is called vorticity axis and the z direction is called velocity gradient axis. When a droplet is deformed under simple shear flow, it changes its shape from spherical to ellipsoidal. Therefore, when it's deformed, a droplet requires the knowledge of its three semi-axis a , b and c in order to evaluate its volume and external surface while for an undeformed spherical droplet the knowledge of its radius R is sufficient. The semi-axes a and b can be measured along the vorticity direction while c is visible along the velocity gradient direction only (see Figure 10). The axis a' is the projection of a along the velocity gradient axis. Finally the angle between the semi-axis a

and the flow direction is defined orientation angle θ and can be observed along the vorticity direction only.

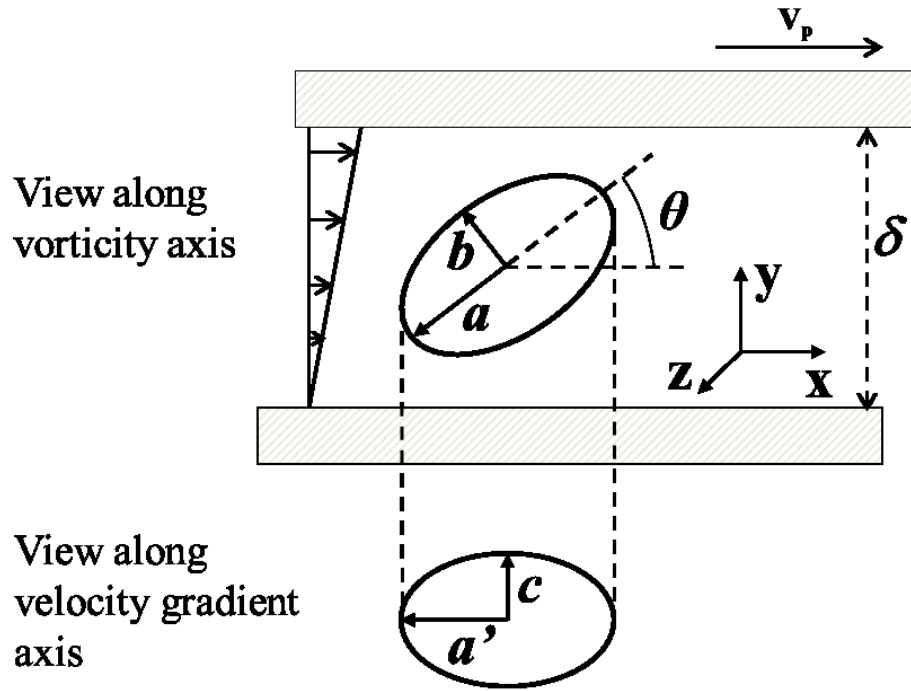


Figure 10. Schematic of simple shear flow.

2.1.1. Taylor theory

The first theoretical studies on the deformation of a single droplet of two immiscible newtonian fluids under simple shear flow were carried out by Taylor.^{26, 66} He solved the differential equations of the creeping motion for undeformed droplet under shear flow, determining that droplet deformation depends on two dimensionless parameters only:

$$\text{Capillary number } Ca = \frac{\eta_c \dot{\gamma} R}{\sigma}$$

$$\text{Viscosity ratio } \lambda = \frac{\eta_d}{\eta_c}$$

where:

η_c and η_d are the viscosities of continuous and dispersed fluid respectively;

R is the radius of the undeformed droplet;

$\dot{\gamma}$ is the shear rate;

σ is the interfacial tension of the two immiscible fluids.

The capillary number represents the ratio between the viscous stress $\eta_c \dot{\gamma}$ due to the shear flow which tends to deform the droplet and the interfacial stress σ / R which tends to maintain the undeformed shape of the droplet.

Taylor found a linear dependence of the drop steady state deformation parameter $D = (a-b) / (a+b)$ with the capillary number Ca in the limit of small deformation (i.e. $Ca \rightarrow 0$).²⁶

$$D = \frac{19\lambda+16}{16\lambda+16} Ca \quad (2)$$

The equation (2) allows an easy calculation of the interfacial tension σ of the pair of fluids. Indeed it states that, in the limit of small deformation, the dependence of the deformation parameter D with the shear rate $\dot{\gamma}$ is linear. Therefore it is possible to obtain the measure of the interfacial tension from the slope of the trend of D with $\dot{\gamma}$ once the other parameters are known.

2.1.2. Cox theory

Taylor theory was later developed by Cox⁶⁷ who studied the dependence of D and of the orientation angle θ with Ca for $\lambda > 1$ under simple shear flow.

Cox found the following correlations:

$$D = \frac{5(19\lambda+16)}{4(1+\lambda)\sqrt{(19\lambda)^2+(20/Ca)^2}} \quad (3)$$

$$\theta = \frac{\pi}{4} - \frac{1}{2} \tan^{-1} \frac{19Ca\lambda}{20} \quad (4)$$

Equations (3) and (4) show a levelling off of the trends of D and θ at the highest values of Ca while they recover the linear dependence in the limit of small deformation (i.e. $Ca \rightarrow 0$) as previously shown by Taylor.

Moreover Cox studied the trend of the deformation parameter D with time t observing the behaviour of the droplet in a time-dependent simple shear flow.⁶⁷ The following correlation in the limit of small deformation (i.e. $Ca \rightarrow 0$) was found:⁶⁷

$$D_t = D \left[1 - 2 \exp\left(-\frac{20\dot{\gamma}t}{19Ca\lambda}\right) \cos(\dot{\gamma}t) + \exp\left(-\frac{40\dot{\gamma}t}{19Ca\lambda}\right) \right] \quad (5)$$

where D_t is the transient deformation parameter. Equation (5) predicts the presence of damped oscillations in the trend of D_t during the start-up of the deformation until a steady state value is reached. The Cox theoretical predictions were experimentally confirmed in a later work⁶⁸ where a good agreement with equations (3) and (4) was found while only a qualitative agreement with equation (5) was shown. In fact the predicted damped oscillations were observed but there is a phase shift between the predicted and the experimental period of the oscillations. This discrepancy is due to the fact that equation (5) was developed $Ca \rightarrow 0$, while the experiments were performed at $Ca \neq 0$.⁶⁸

2.1.3. Retraction theory

The retraction of a deformed drop back to the spherical, equilibrium shape at rest has been the subject of several studies in the literature.⁶⁹ In particular the retraction of a drop deformed under the action of a shear flow was analysed by using the theoretical approach proposed by Rallison in the limit of small deformations.⁶⁹ A single exponential decay was then obtained for the time evolution of the deformation parameter in the course of retraction as follows:⁶⁹

$$D_t = D \exp\left(-\frac{40(\lambda+1)}{(2\lambda+3)(19\lambda+16)} \frac{t\sigma}{\eta_c R}\right) \quad (6)$$

According to equation (6), data of $\ln(D_t / D)$ vs t should fall on a straight line and the scaling of droplets with different radii should be obtained with the first power of the radius R .

2.2. Tube flow

The first theories regarding the drop deformation were developed under simple shear flow. Later other kinds of flow were studied in order to understand the behaviour of the immiscible fluids in condition more similar to industrial applications. An important type of flow is the one occurring in a tube of circular cross section when the inertial stresses are negligible. The geometry of the tube is represented in Figure 11. The tube has length L and radius R_t and the fluid moves from top to down due to a pressure difference $\Delta P = P_0 - P_L$ between the edges.

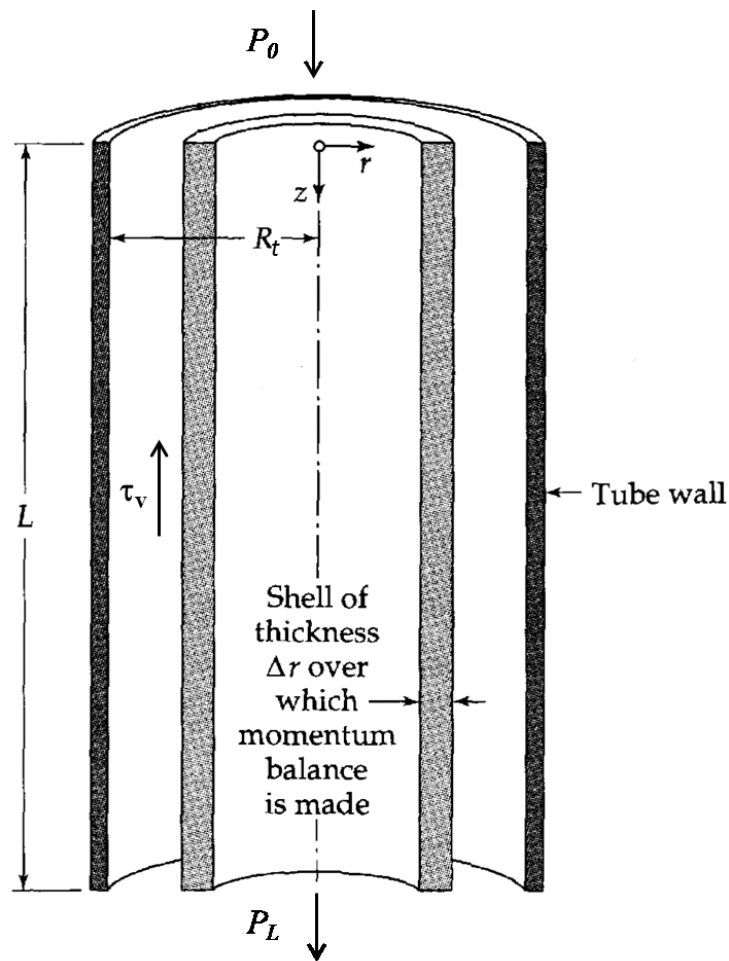


Figure 11. Tube of circular cross section⁷⁰

A system of cylindrical coordinates, $r - z$ where z is the direction of flow and r is the radial direction, is used as reference system. Then it is possible to perform a balance of forces on an infinitesimal annular volume control, limited by two cylinders of length L and radius equal to r and $r + dr$ respectively. The only forces acting on the volume control along the axial direction are those due to the pressure the viscous stress τ_v along the lateral cylindrical surfaces(see Figure 11). Then the balance of forces along the z direction provides:⁷⁰

$$2\pi r dr(P_o - P_L) + 2\pi r L \tau_v|_{r+dr} - 2\pi r L \tau_v|_r = 0$$

and subsequently:

$$\frac{d}{dr}(r\tau_v) + \frac{(P_o - P_L)}{L} r = 0$$

Integrating this differential equation we obtain the stress profile along the tangential direction:

$$\tau_v = \frac{\Delta P}{L} \frac{r}{2} + \frac{C_1}{r}$$

The constant of integration C_1 must be zero, for otherwise the momentum flux would be infinite at the axis of the tube.⁷⁰ The resulting equation will be:

$$\tau_v = \frac{\Delta P}{L} \frac{r}{2} \quad (7)$$

Equation (7) shows a linear dependence between the stress τ_v and the radius r of the tube. Depending on the type of fluid, the stress can be expressed through an appropriate constitutive equation.

2.2.1. Newtonian fluid

The stress τ_v for a newtonian fluid of viscosity η is expressed by the following Newton's law of viscosity:

$$\tau_v = \eta \left(\frac{dv}{dr} \right)$$

Substituting this relation in the equation (7) the following differential equation is obtained:⁷⁰

$$\eta \frac{dv}{dr} = - \frac{\Delta P}{L} \frac{r}{2}$$

This first-order separable differential equation may be integrated to give:⁷⁰

$$v = -\frac{\Delta P}{4\eta L} r^2 + C_2$$

The constant C_2 is evaluated considering that $v = 0$ at $r = R_t$ as boundary condition. Then the velocity distribution for laminar incompressible flow of a Newtonian fluid in a long tube is:⁷⁰

$$v = \frac{\Delta P}{4\eta L} R_t^2 \left(1 - \frac{r^2}{R_t^2}\right) \quad (8)$$

The volumetric flow rate Q is obtained through a second integration.⁷⁰

$$Q = \int_0^R v 2\pi r dr = \frac{\pi R_t^4 \Delta P}{8\eta L} \quad (9)$$

Equation (9) is known as Hagen-Poiseuille equation and is valid only for a newtonian fluid in laminar flow.⁷⁰

2.2.2. Non-newtonian fluid

In the case of non-newtonian fluid the relationship between the stress τ_{rz} and the fluid viscosity can be described by several models. One of the most used is the power-law model. For this model, the constitutive relation is:⁷⁰

$$\tau_v = K \left(\frac{dv}{dr}\right)^n$$

Replacing this relation in the equation (7):⁷⁰

$$K \left(\frac{dv}{dr}\right)^n = -\frac{\Delta P}{L} \frac{r}{2}$$

Integrating and using the same boundary condition of the newtonian case the following velocity profile can be obtained:⁷⁰

$$v = \frac{n}{n+1} \left(\frac{\Delta P}{2KL} \right)^{\frac{1}{n}} \left(R_t^{\frac{n+1}{n}} - r^{\frac{n+1}{n}} \right) \quad (10)$$

and the volumetric flow rate Q is:⁷⁰

$$Q = \int_0^R v 2\pi r dr = \frac{\pi n}{1+3n} \left(\frac{\Delta P}{2KL} \right)^{\frac{1}{n}} R_t^{\frac{1}{n}+3} \quad (11)$$

In the case of $n = 1$ the equations (8) and (9) for a newtonian fluid are recovered. Instead for $n \neq 1$, the viscosity is no more constant with the shear rate $\dot{\gamma}$ as in the newtonian case; if $n < 1$ the fluid has a shear-thinning viscosity while if $n > 1$ the viscosity is shear-thickening.

2.2.3. Hetsroni theory

Regarding the behaviour of a single droplet of two immiscible newtonian fluids under capillary flow (i.e. laminar tube flow) an important work is the Hetsroni study.⁷¹ He used the method of reflection to solve the flow fields inside and around an undeformed droplet under Poiseuille flow obtaining the following correlation in the limit of small deformation (i.e. $Ca \rightarrow 0$) and small confinement (i.e. $k \rightarrow 0$):⁷¹

$$\frac{U}{V_m} = 2 - \frac{4\lambda}{3\lambda+2} \cdot \kappa^2 + O(\lambda^3) \quad (12)$$

where:

U is the velocity of an axial-symmetric droplet;

V_m is the mean velocity of the Poiseuille velocity profile;

k is confinement degree defined as $k = R / R_t$ where R is the radius of the undeformed droplet and R_t is the capillary radius.

The element $O(\lambda^3)$ is a higher order infinitesimal and then can be neglected. Equation (12) states that the velocity of the droplet decreases as its dimension approaches the capillary dimension while there is a weak dependence on the viscosity ratio λ . Hetsroni theory was experimentally validated by other works^{72, 73} where the velocity of the droplets was investigated and the flow fields inside and around the droplets were observed.⁷³

3. Experimental section

3.1. Materials

3.1.1. Multilamellar vesicles

The material used in this work is an aqueous solution of the commercial anionic surfactant linear alkylbenzenesulfonic acid (HLAS). In Figure 12 the chemical structure of the HLAS molecule is shown. It can be seen the presence of the benzene ring linking a sulphonic acid group (hydrophilic head) and a linear alkyl group (hydrophobic tail).



Figure 12. HLAS chemical structure.

The phase diagram of HLAS – water solution shows three different regions depending on HLAS concentration and the temperature as shown in Figure 13.

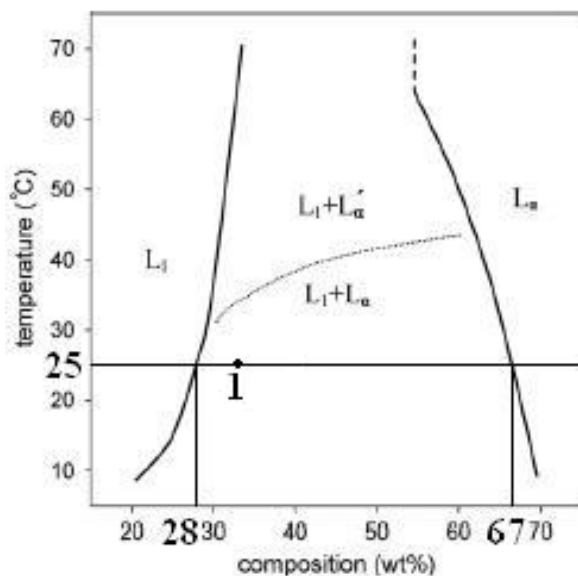


Figure 13. Phase diagram of the HLAS – water system.

Regarding the temperature all the observations were done at room temperature ($\approx 25^\circ \text{C}$). At this temperature the diagram shows that at low HLAS concentration ($< 28\% \text{ wt.}$) the isotropic micellar L_1 phase is present only, while the lamellar L_α phase is the only one present at the highest concentration ($> 67\% \text{ wt.}$). Between them there is the coexistence of both L_1 and L_α phase and SMLVs can be found.^{74,75} Our samples were provided from Procter and Gamble (Pomezia Technical Center, ing. Vincenzo Guida) and have a concentration of 33% wt. of HLAS. They show SMLVs of different size (ranging from a few to hundreds of micron) which can be

easily observed under optical microscopy, in both bright field and polarized light.

3.1.2. Buchwald-Hartwig reaction

The [Pd(NHC)] pre-catalyst [Pd(IPr*)(cin)Cl] (**1**) was prepared according to the procedure reported in the literature.⁶⁰ Potassium tert-pentoxide (KOTAm) was received as a solution in toluene (Aldrich, technical, ~25% in toluene), then vacuum dried under inert atmosphere and used as a dried white powder under inert atmosphere. 1-methylpiperazine (Aldrich, 99%), 1-bromo-2,4-dimethylbenzene (Aldrich, 97%), 4,4'-di-tert-butylbiphenyl (Aldrich, 99%), decane (Aldrich, ≥99%), toluene (Aldrich, anhydrous, 99.8%), 1,2-dimethoxyethane (DME) (Aldrich, puriss., dried over molecular sieves (H₂O ≤0.005%), ≥99.5%) were used as purchased.

3.2. Methods

3.2.1. Rheology

The rheological measurements of the sample were carried out at room temperature by a stress controlled rotational MCR 301 rheometer (Anton Paar Instruments). A cone-plate 1°/75 mm geometry was used loading 2,5 ml of solution. Both continuous and oscillatory flow tests were performed.

3.2.2. Flow Cell

The rheo-optical apparatus used in this work, which is described in detail elsewhere,^{76,77} consists essentially of a shear cell coupled with an optical microscope (Axioscope) equipped with a high speed video camera

(Phantom 640) and a motorized focus system. The microscope itself is mounted on a motorized translating stage, which was used to keep the SMLVs within the field of view during the experimental runs. In all the experiments, observations were performed in bright field and polarized light, using long working distance optics (10x, 20x). The whole apparatus is placed on a vibration-isolated table and can be operated in two different, interchangeable setups to observe the sample either along the velocity gradient or along the vorticity direction. In either setup, simple shear flow is generated by displacing the motorized plate with respect to the other one, once the opposing surfaces are properly aligned by using a set of rotary and tilting micrometric stages. The misalignment is typically less than 5 μm over the entire surface of the plates. The gap between the plates can be adjusted by means of micrometric stages. Shear rates $\dot{\gamma} = v_p/\delta$ where v_p is the velocity of the moving plate and δ is the gap between the two plates (Figure 14) were set in the range 0.1 – 10 s^{-1} in order to investigate the dynamic behaviour of SMLVs. The experimental deformation of the SMLVs is described by using the deformation parameter $D = (a - b)/(a + b)$ where a and b are, respectively, the major and minor axis of the deformed droplet and the orientation angle θ between the major and the flow axis in the sheared plane (Figure 14). A deformation parameter $D' = (a' - c)/(a' + c)$, where a' is the projection of the major axis a and c is the third axis of the deformed SMLV, is defined along the velocity

gradient view as well as in the vorticity one as shown in Figure 14. The three axes are measured by using image analysis techniques.

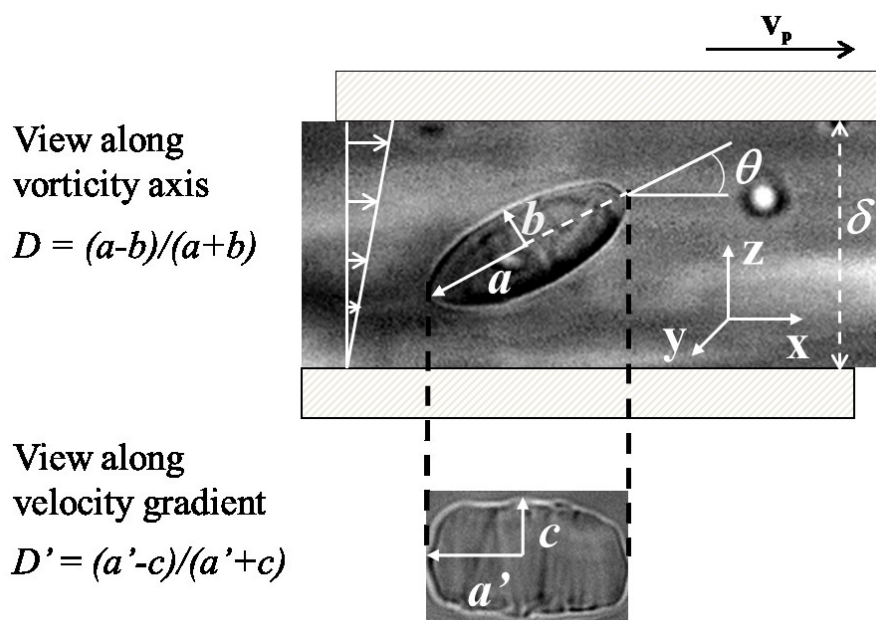


Figure 14. Schematic of the parallel plate apparatus showing the two directions of observation (vorticity axis and velocity gradient).

3.2.3. Capillary flow

The analysis of the fluid dynamics and deformability of SMLVs under capillary flow was performed by using an experimental apparatus made up of silica micro-capillaries with a circular section. Those were bought by Polymicro Technologies and have an inner diameter comparable to the average size of vesicles. In particular, the experiments were run by using micro-capillaries with an inner diameter D_c equals to 106 μm , 180 μm , and 318 μm respectively. A syringe pump (Harvard 11 Plus) was used in order to inject the HLAS solution in the micro-capillaries. This syringe pump allows to obtain flow rates ranging from 0.0010 l / hr to 30 ml / min. The

syringe pump and the micro-capillaries were connected by suitable connections. Images of SMLVs flowing inside the micro-capillaries were acquired by a high speed video camera (Phantom 640) and analysed later. In all the experiments, observations were performed in bright field and polarized light, using long working distance optics (10x, 20x). Finally the whole apparatus is placed on a vibration-isolated table as shown in Figure 15.

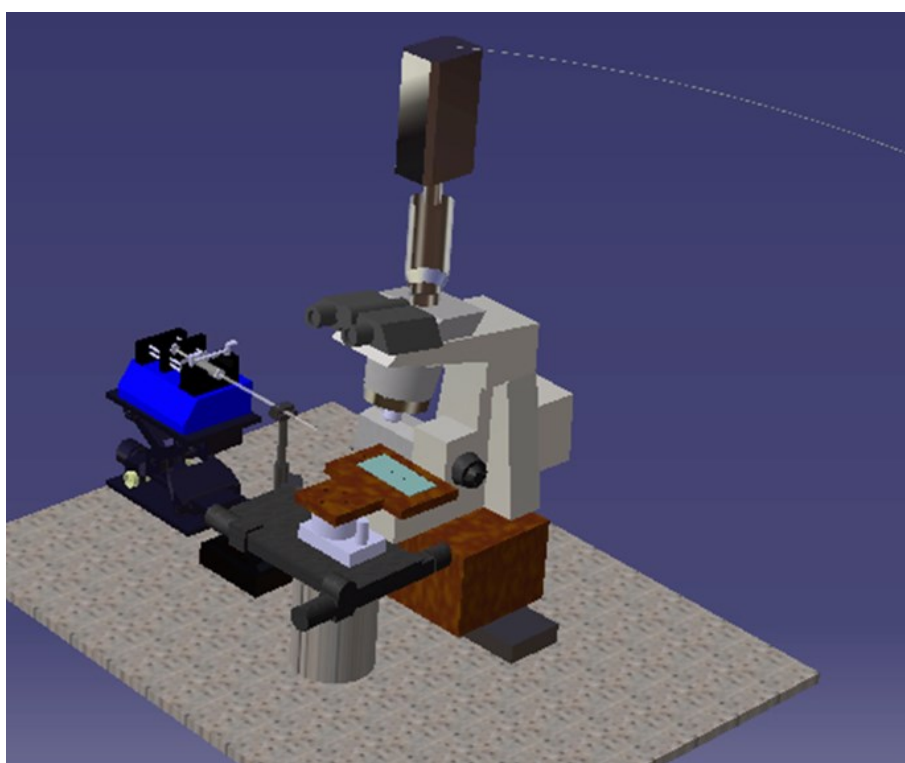


Figure 15. Experimental apparatus used for the capillary flow.

3.2.4. Image analysis

The study of the parameters relating to the deformation of the vesicles subjected to shear flow has been carried out on the images acquired in real time from the camera and transferred to the computer in digital format using

the commercial software Image Pro Plus 7. The analysis of the acquired images consists in the determination of certain geometrical quantities of the vesicles deformed on the basis of the assumption that the shape of the vesicles is in good approximation ellipsoidal. In particular, an algorithm based on grey levels allows the identification of the outline of the droplet, which is darker than the rest because of the difference of the refractive indices of the two fluids.

The analysis process of the image sequences can be divided in the following way:

1. Acquisition of single images.
2. Evaluation of the geometric fundamental
3. Evaluation of the characteristic parameters of the deformation

During the analysis of the deformation many difficulties have been encountered. A problem regards the issue of the calibration of the microscope. In fact, the program Image Pro Plus requires the calibration factor $\mu\text{m} / \text{pixels}$ that converts the measurements made in pixels in quantities expressed in microns. The factor $\mu\text{m} / \text{pixel}$ depends on the objective and the microscope used. Generally, if you proceed to the analysis of the vesicles directly on the program by setting the calibration, the values come out in microns; the risk is that, in case of a mistake with the optics, there is no possibility to correct the values and a repeat of the measure is needed. In order to avoid this risk, the values were processed directly in pixels and multiplied by the conversion factor only later.

Another source of error is the criticality of the analysis of the orientation angles θ of the vesicles subjected to shear flow along the vorticity view. A first difficulty was to understand what angle the image analysis program Image Pro Plus read: the one between the axis parallel to the flow axis and the principal one of the deformed vesicle or its complementary? To verify this hypothesis, we carried out the manual analysis of some experiments in the frame of view vorticity and we compared the results with the ones of the automatic analysis. Often manual analysis proved to be more accurate and therefore preferable, while other times has been less necessary. The manual analysis requires time and attention: the image is selected, copied and pasted as a new frame (new pasta), then you need to resize, and after to turn it. The resize is necessary because the pixel is rectangular, in particular the height is greater than the base of 4%, and therefore it must be resized into a square form to not deform the image during the rotation. After turning the vesicle, an ellipse was fit on the vesicle using the note of the Image Pro Plus. You can choose a colour for the outline based on the mask and make the measurements of the quantities required by the count and measurement object. Manual measurement for a vesicle along the gradient view is much easier. You can copy and paste the image as a new frame, then, using the tools of note, adapts the ellipse equivalent and measure. Beyond the technical problems related to the proper use of the software, the real obstacles are the experimental ones. Some common problems are:

1. Lack of pictures with vesicles relaxed;

due to the fact that the vesicles were lost during the run or by other vesicles. In these cases we can resort to an approximate calculation of the radius for conservation of volume equalling the volume of the ellipsoid of rotation (form assumed by the vesicle in flow) with the volume of the sphere (geometry of the vesicle relaxed) only if the vesicle is in the vorticity view. Instead, for a vesicle along the gradient view, the same calculation is bogus because what you see is the projection on the sliding plane and not the real drop.

2. Uncertainty in defining the vesicle contours;
due to a poor focus of the images or the turbidity of the solution that is highly concentrated. In these cases we resort to common sense and we considered a contour line intermediate.
3. Lens effect;
this is a problem caused by the reflection of the neighbouring vesicles that are behind or ahead of the vesicle immediately analysed. This effect can damage the analysis of vesicles because it alters the perception that one has of the boundaries of the vesicle.
4. Difficult to assess the orientation angle;
regarding the manual analysis, the human eye has an indecision of $\pm 1^\circ$ in the decision of the orientation angle (this value it was evaluated by a mean of several repetitions of the same measurement).
5. Uncertainty ellipsoid;

because often large vesicles subjected to high shear rate can assume strange shapes (elongated as meteoric or curved form). In this case, the images are discarded, but there are also many intermediate situations where the vesicle seems almost ellipsoidal. One possible method of verification may be the use of the option of the count and measurement object / Outline style / Ellipse that translates the images to read colour contrast in ellipses equivalent.

3.2.5. Confocal microscopy

An investigation of the internal structure of SMLVs was performed by the Laser Scanning Confocal Microscopy (LSCM) technique. A fluorescent marker (Rhodamine B , 1 $\mu\text{g/ml}$) was added to HLAS solution to make a 3D reconstruction of the SMLVs using a commercial software of image analysis software package (Image Pro Plus 7). The confocal microscope was a Zeiss LSM 5 PASCAL. It's made by the transmitted light microscope Axiovert 200 M equipped with a high resolution digital camera AxioCam and a high magnification optics (40x, 63x) were used. The module of the laser comprises a first Ar laser emitting at three different wavelengths (458, 488, 514 nm) and a second HeNe laser emitting at a wavelength of 543 nm. The scanning module comprises a confocal pinhole with a variable diameter and a channel equipped with high sensitivity PhotoMultiplier Tubes (PMT) for the detection of the signal. There is also an additional channel for detecting the transmitted light.

3.2.6. Batch reactor

In a glovebox, dry KOtAm (1.1 M) was added in a vial equipped with a stirring bar and sealed with a screw cap fitted with a septum. Outside the glovebox, 1-bromo-2,4-dimethylbenzene (1 M), N-methylpiperazine (1.1 M), decane (0.13 M) as internal standard and finally a solution of **1** (prepared inside the glovebox in 1 mL of DME, 0.0012 – 0.01 M, 0.12 - 1 mol %) were added. The reaction mixture was then stirred (800 rpm) at 50°C. Aliquots were taken under nitrogen with a syringe through the septum at appropriate times. The conversion of the aryl-bromide was determined by GC.

3.2.7. Continuous flow reactor

A scheme of the flow system is shown in Figure 16. The reagents were injected into the microreactor with two syringes placed on the same syringe pump (Harvard Pump 11 Plus Dual), in order to impose the same flow rate at both of them. In particular, the flow rate was varied from 0.1 ml/hr to 300 ml/hr, in order to have different residence times. A solution of **1** in DME or toluene as solvent, prepared inside the glovebox under inert atmosphere in the concentration range from $0.26 \cdot 10^{-3}$ M (0.12 mol %) to $2.22 \cdot 10^{-3}$ M (1 mol %), was loaded in the first syringe. The second syringe was charged with a solution (once again prepared inside the glovebox) made of 1-methylpiperazine (0.24 M) as the amine, 1-bromo-2,4-dimethylbenzene (0.22 M) as the ArBr, 4,4'-di-*tert*-butylbiphenyl (0.01 M) as the internal standard and potassium *tert*-pentoxide (0.24 mM) as base in either DME or

toluene as solvent. The mixing of the two solutions was performed in a stainless steel 1 mm i.d. T-junction and the reaction took place in a stainless steel tubular microreactor. Because of the generation of potassium bromide (KBr) during the reaction two microreactors with different inner diameters and lengths were used to overcome the possible clogging of the microreactor as described in the results. The narrow-bore tube is of 1 mm i.d. and 1.5 m length (volume = 1.18 ml) and the wide-bore tube is of 2.0 mm i.d. and 0.70 m length (volume = 2.2 ml). The microreactor and the T-junction were heated in a thermostatic bath at two different temperatures, 30°C and 50°C, while both the syringes containing substrates and catalyst are at room temperature. The effluent was analysed by GC in order to determine the conversion of the aryl-bromide and the presence of potential by-products. Controls in absence of the catalyst were carried out to investigate the possible substrate adsorption inside the microreactor. The results confirmed that adsorption was negligible.

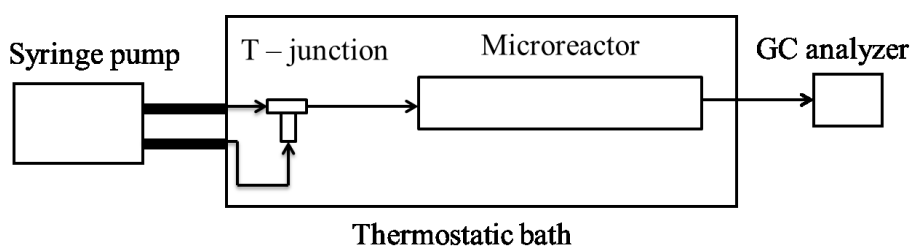


Figure 16. Scheme of the continuous flow reactor.

3.2.8. Analytical method

Concentrations of the amine and the aryl bromide were determined by Shimadzu GC-FID 2010 with a non-polar capillary column (BPX5 10 m,

i.d. 0.1 mm, 0.1 μm film thickness from SGE). Gas carrier was He, with a linear velocity of 50 cm/s, injector and FID detector temperatures were set to 320° C and 360° C, respectively. 1 μL of sample was injected in splitless mode. Column temperature was kept at 50° C for 3 min, then risen by 30° C/min up to the final temperature of 360° C, and kept at this value for 6 min.

4. Results and discussions

4.1. Vesicle behaviour under simple shear flow

4.1.1. Rheological results

In Figure 17 continuous and oscillatory rheological data of 33% wt. HLAS solutions are shown.

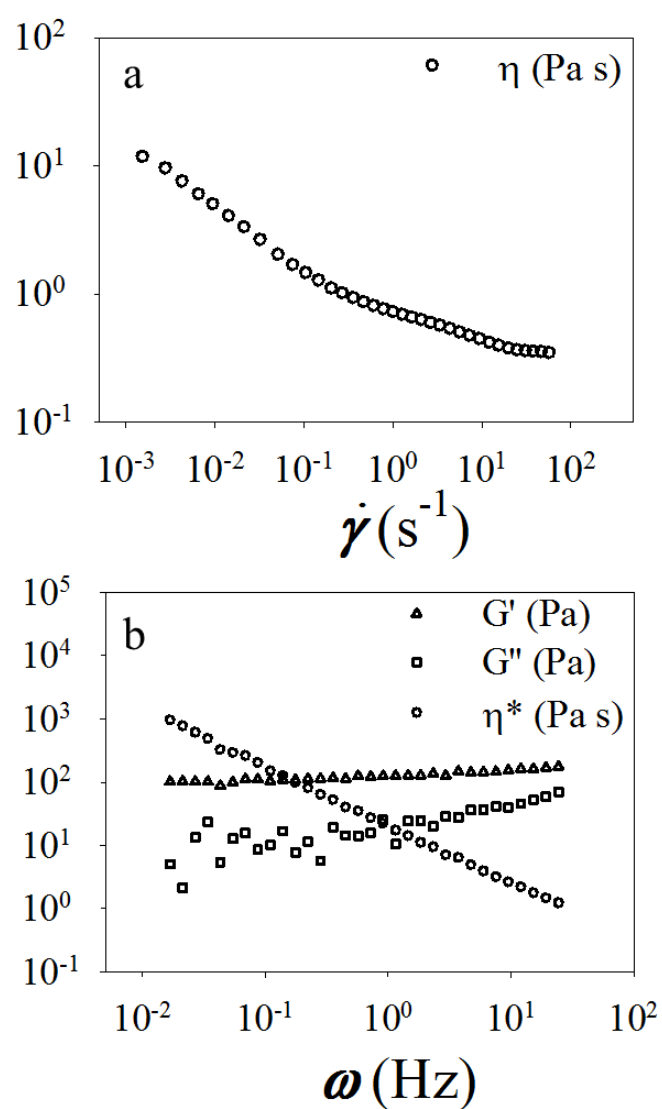


Figure 17. Rheological data of HLAS sample: flow curve (a) and frequency sweep (b).

The flow curve in Figure 17a shows that the sample has a shear-thinning viscosity in the range of shear rates of interest for our experiments and its viscosity can be then considered by using the power law model. However it is interesting to observe that the shear-thinning part shows two different slopes in the entire range of shear rate investigated. Therefore it was possible to obtain a value of the power law index n for the two ranges of shear rate. In the first range ($10^{-3} - 0.15 \text{ s}^{-1}$) the fitting of the data gives a power law index $n = 0.48$ while in the second range ($0.15 - 50 \text{ s}^{-1}$) a value of 0.79 is achieved. In Figure 17b the elastic and viscous moduli from oscillatory tests are plotted as a function of frequency together with the complex viscosity. The latter exhibits a shear-thinning behaviour in qualitative agreement with the flow curve (it should be noticed that the Cox-Mertz rule does not hold for this system, i.e., continuous and oscillatory viscosity data do not superimpose at the same frequency/shear rate). Furthermore, G' is always higher than G'' in the entire range of frequency investigated, thus indicating a dominant elastic component in the rheological response. This can be due to the presence of both lamellar phase and multilamellar vesicles in the HLAS sample investigated.⁷⁸

4.1.2. Dynamic behaviour

Representative images of sheared SMLVs under steady-state conditions are shown in Figure 18. In the top image sequence (a), a vesicle sheared at a low value of $\dot{\gamma}$ rotates without appreciable deformation (tumbling) as observed along the vorticity axis. In the following sequence (b), a periodic

deformation can be noticed, with a rotation accompanied by compression and extension in the corresponding quadrants of the shear flow, similar to the breathing motion observed for unilamellar vesicles. The last two sequences, (c) and (d), refer to two vesicles of comparable size as observed along the vorticity and velocity gradient axes, respectively. In sequence (c), starting from a quasi-spherical shape at rest, the vesicle assumes an ellipsoidal steady-state shape with a continuous rotation of the interface (tank treading), in analogy with a sheared droplet or capsule.

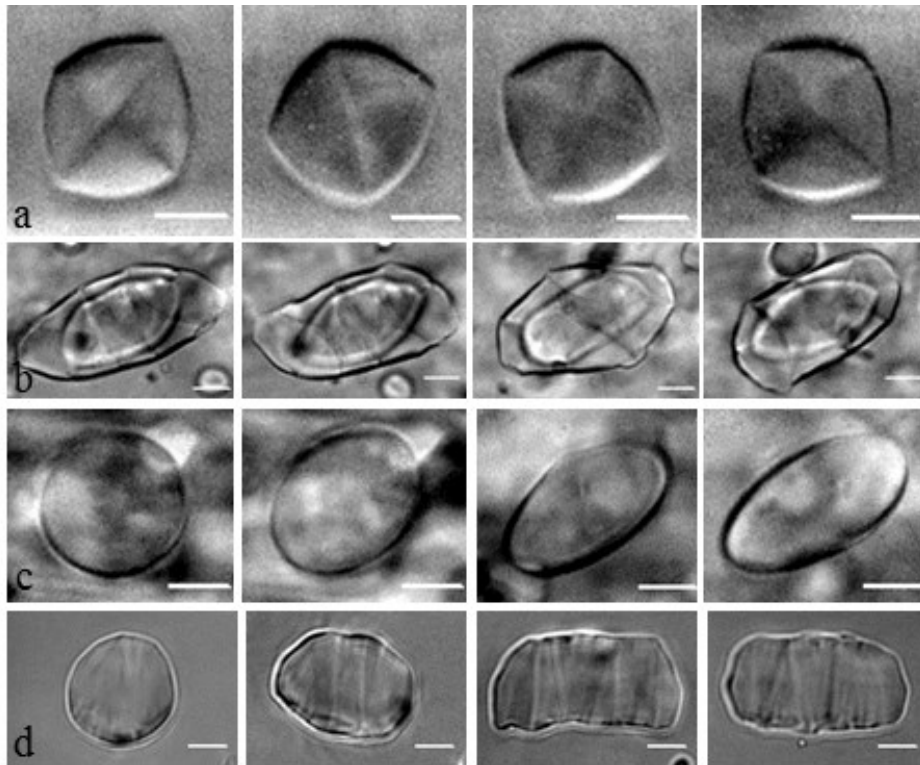


Figure 18. Images of sheared vesicles. View along vorticity axis: a) $\dot{\gamma} = 0.075 \text{ s}^{-1}$; b) $\dot{\gamma} = 0.7 \text{ s}^{-1}$; c) $\dot{\gamma} = 1 \text{ s}^{-1}$. View along velocity gradient: d) $\dot{\gamma} = 1 \text{ s}^{-1}$. Flow direction is from left to right. Scale bar = $30 \mu\text{m}$.

The deformation modes shown in Figure 18 are represented in a quantitative way in Figure 19, where the transient deformation parameter D_t' in the view along the velocity gradient is plotted as a function of non-dimensional time $t^*\dot{\gamma}$ for two vesicles of similar radius. In the top diagram an oscillatory trend is found corresponding to the breathing motion of Figure 18b. In the bottom plot a steady state value of D_t' associated with a tank-treading deformation (such as in Figure 19c and d) is reached after a few damped oscillations. These trends once again share some analogy with the shear deformation of elastic capsules and emulsion droplets (at high viscosity ratios). In the latter case, the presence of a surfactant at the droplet surface can generate more complex behaviours depending on the relative contribution of surfactant elasticity and flow strength.

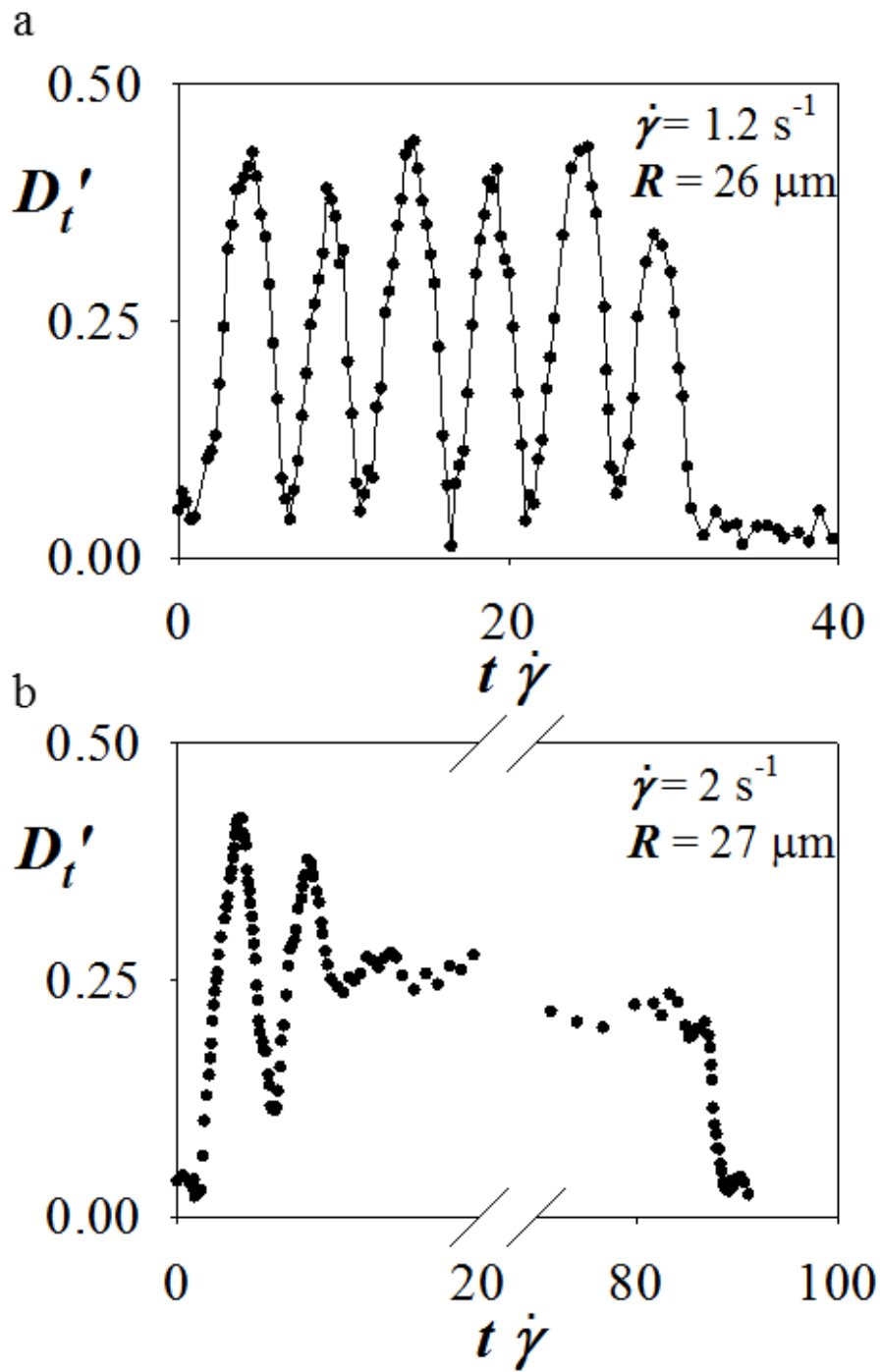


Figure 19. D' vs non-dimensional time $t * \dot{\gamma}$.

Based on these analogies, we investigated whether SMLVs deformation follows a scaling behaviour similar to that of capsules and droplets. As

recognized by Taylor,²⁶ the deformation parameter of isolated droplets is a function of two non-dimensional quantities: the viscosity ratio $\lambda = \eta_d / \eta_c$, where η_d and η_c are the viscosities of the droplet and continuous phase, respectively, and the capillary number Ca , expressing the ratio between shear and interfacial stresses, which is given by $\eta_c \dot{\gamma} R / \sigma$, where R is the droplet radius at rest and σ is the (effective) interfacial tension (for elastic capsules the interfacial tension is replaced by an elastic constant). More support to this approach is given by the work of De Gennes,⁷⁹ who demonstrated that, albeit a single bilayer might have null surface tension, a stack of open bilayers will exhibit a non-zero effective surface tension because of bilayers interaction (this analysis was extended to the case of a closed multilamellar vesicle by Van der Linden and Droge³⁰). The predictions of Taylor theory, though developed for isolated droplets, are still valid for low to moderate concentration emulsions, provided that η_c is replaced by the emulsion viscosity η .⁸⁰ In order to calculate Ca an estimate of the effective interfacial tension σ_{eff} is needed. This was done by fitting Taylor's equation:²⁶

$$D = \frac{19\lambda+16}{16\lambda+16} Ca \quad (2)$$

to data of D vs $\eta_c \dot{\gamma} R$ (only the linear region of the plot, starting from $D = 0.3$ and up to $D \simeq 0.6$, was considered). The so obtained value of σ_{eff} , which is the only fitting parameter (the viscosity ratio being essentially irrelevant in this calculation due to the weak dependence of D on λ), was

10^{-1} mN/m, and falls within the range of theoretical predictions (10^{-2} - 1 mN/m) for a lamellar droplet.³⁰ By using this value of σ_{eff} the capillary number was calculated and the steady state data of D and θ for several vesicles with different radii (ranging from 10 to 100 μm) were plotted as a function of Ca , as shown in Figure 20a and b.

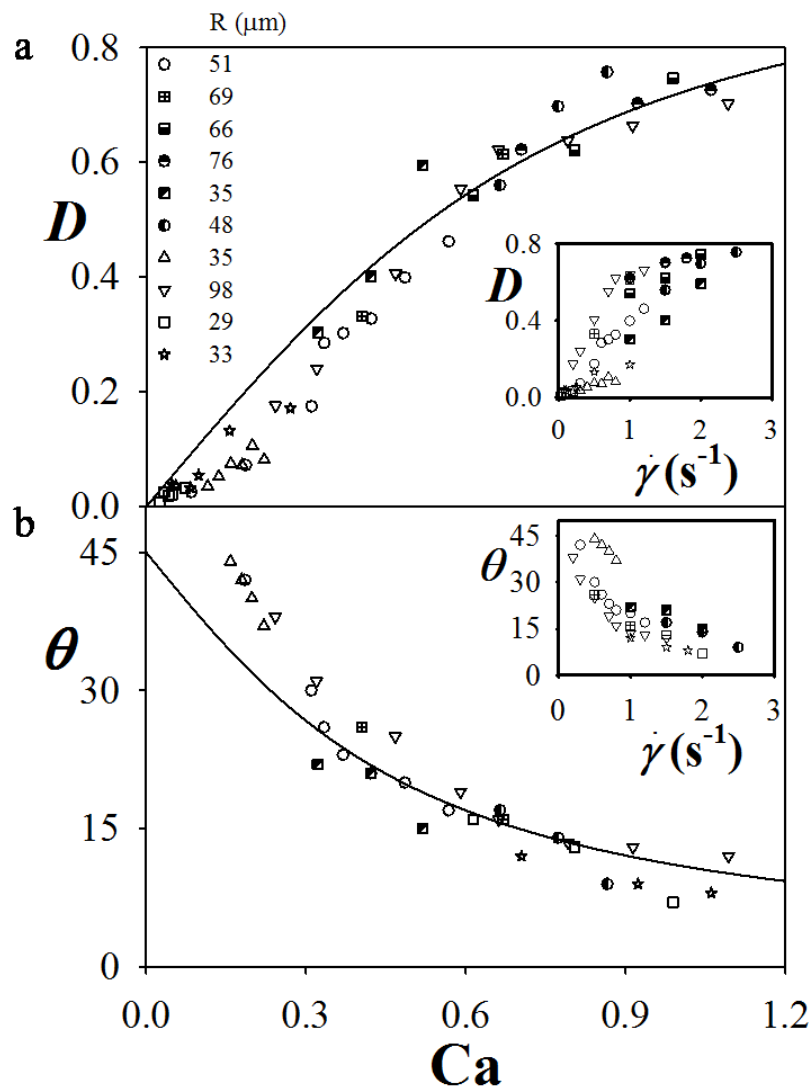


Figure 20. Deformation parameter (a) and orientation angle (b) as a function of the capillary number. Vesicle radius is shown in the legend. The unity slope is shown as a reference in (a). The vertical dashed line shows the transition to the tank-treading regime, which is found at $Ca > 0.3$.

In Figure 20a the linear region, which has been used in the determination of σ_{eff} , corresponds to a slope of 1, as predicted by Taylor's equation. It should be noticed that at low values of Ca up to ≈ 0.3 a different slope is apparent. This region corresponds to tumbling (up to $Ca \approx 0.1$) and breathing motion ($0.1 \leq Ca \leq 0.3$). At higher values of Ca , where tank-treading deformation is observed, a levelling off of D can be noticed. The good scaling of the experimental data with the capillary number can be appreciated from the inset of Figure 20a, where the deformation parameter is plotted vs the shear rate only. Such scaling with radius provides further support to our estimate of the effective interfacial tension and is qualitatively different from the case of unilamellar vesicles, where data scale with R^3 since the main elastic constant is the bending modulus.⁸¹

In Figure 20b the orientation angle θ is plotted as a function of Ca . Once again, data scale with Ca , as shown by the inset. θ values at low Ca , where the SMLVs exhibit tumbling and breathing motion, are missing since the orientation angle is undefined. At high values of Ca the angle θ tends to zero as expected. Taylor analysis, being developed under the assumption of small deformations, does not predict the levelling off of D at high values of Ca , nor the decrease of the orientation angle with Ca . These features are captured by a later extension of Taylor theory to $\lambda > 1$ due to Cox.⁶⁷ The prediction of Cox theory for D and θ are as follows:⁶⁷

$$D = \frac{5(19\lambda+16)}{4(1+\lambda)\sqrt{(19\lambda)^2+(20/Ca)^2}} \quad (3)$$

$$\theta = \frac{\pi}{4} - \frac{1}{2} \tan^{-1} \frac{19Ca\lambda}{20} \quad (4)$$

The continuous lines in Figure 20a and b are fit of Cox predictions according to equation (3) and (4), respectively, where the only fitting parameter is the viscosity ratio (σ_{eff} being set to the value of 10^{-1} mN/m already calculated). The so obtained value of λ , which is around 2, should be taken as an average quantity due to the shear thinning of the surfactant solution viscosity. By fitting the Cox theory to D at low capillary numbers only, values of $\lambda \gg 1$ were found. In this range of viscosity ratio Cox theory predicts a damped oscillatory behaviour for sheared droplets,^{67, 68} which is similar to the transient data of Figure 19b.

In Figure 21 the three axes made non-dimensional with respect to the radius R are plotted as a function of Ca (a/R and b/R were measured in the view along the vorticity axis, while c/R was obtained from the view along the velocity gradient). The continuous lines are parabolic fits to the data, according to the theoretical predictions for droplet shape based on second order expansion in the capillary number, such as Cox analysis. The vesicle non-dimensional volume V , calculated as the product of the three non-dimensional axes (i.e., abc/R^3), is shown as a function of Ca in the inset of Figure 21. All the data collapse around a horizontal line at a value of $V = 1$, thus showing that the volume is preserved during deformation.

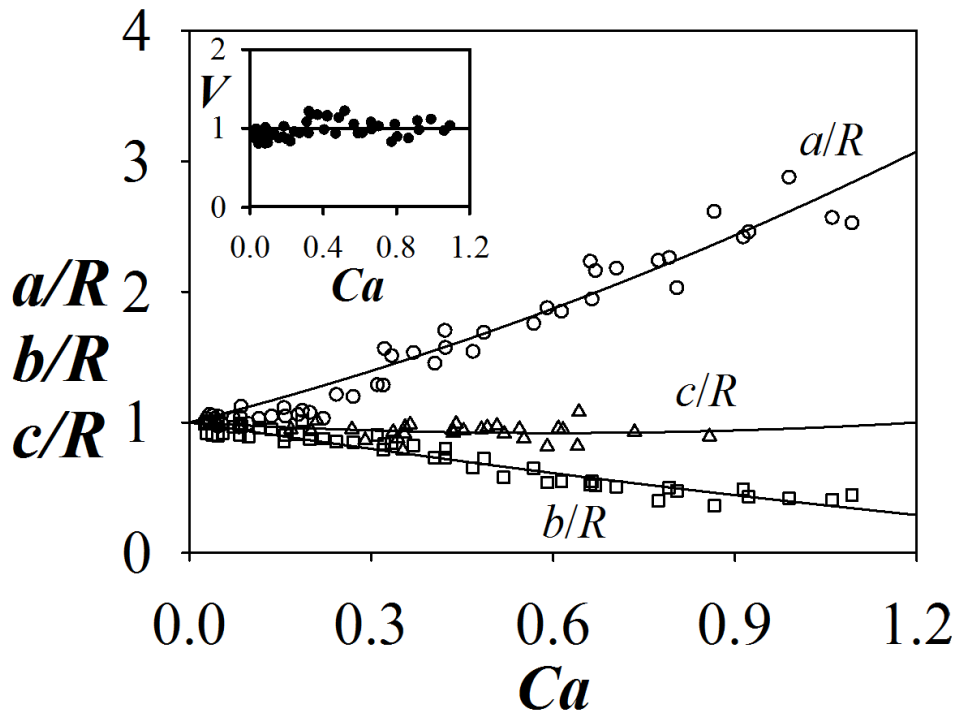


Figure 21. Vesicle dimensionless axes as a function of the capillary number.

The high steady-state values of D in Figure 20a are somehow surprising for SMLVs, since deformation should be limited due to the lack of flow-induced generation of new surface. In order to elucidate this point, vesicle shape at rest was investigated by confocal microscopy.

4.1.3. Internal structure

Typical images of SMLVs are shown in Figure 22 both under confocal (a, c) and polarized light (d) microscopy.

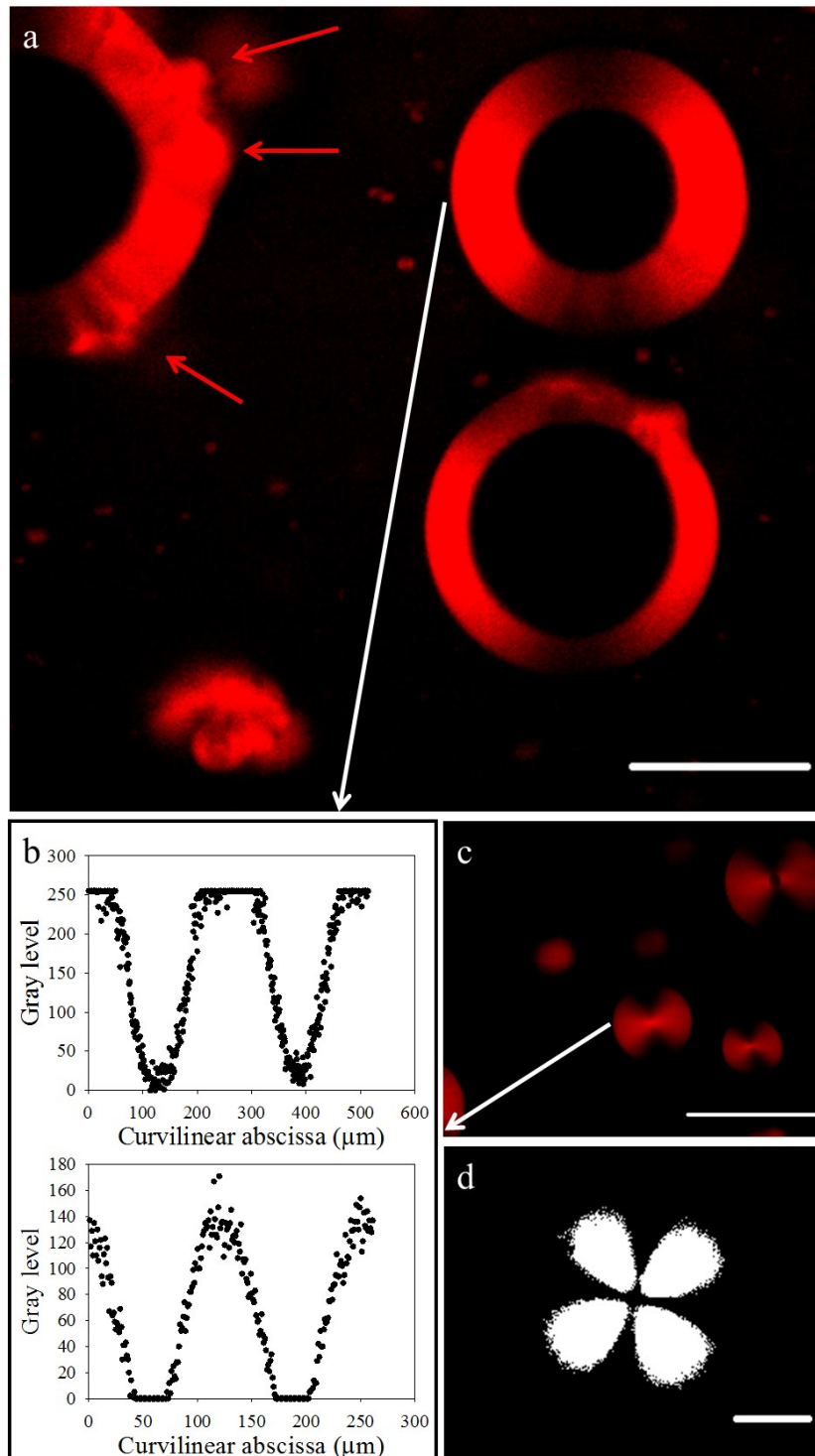


Figure 22. a), c) Images of SMLVs under confocal microscopy at rest. Dimensional bars represent $50 \mu\text{m}$. b) Intensity profiles along the circumference of two vesicles (shown by the white arrows) with radius $42 \mu\text{m}$ (top) and $15 \mu\text{m}$ (bottom). d) A Maltese cross exhibited by a SMLV observed under polarized light at rest. Dimensional bar represents $10 \mu\text{m}$.

The images taken in confocal microscopy show the presence of different size populations of SMLVs. In Figure 22a SMLVs with a large internal dark core and a bright outer shell are seen. The former can be interpreted as a pool of micellar phase such as the one surrounding the vesicles. The presence of an internal pool in SMLVs has been postulated in previous studies, although direct observations are lacking. The outer shell can be associated with a lamellar phase made of a stack of surfactant bilayers. The brightness of the shell comes from a higher Rhodamine concentration in the lamellar region where surfactant concentration is higher than in the continuous micellar phase. A further evidence that the bright shell corresponds to a lamellar structure is provided by the sinusoidal intensity patterns along the vesicle circumference which is shown in the top of Figure 22b. Such pattern is due to a fluorescence polarization effect associated with the ordered radial microstructure of the surfactant bilayers. Another interesting feature of Figure 22a is the presence of some heterogeneity in the outer shell of some SMLVs (see red arrows), which is likely generated by vesicle coalescence. In fact, flow-induced merging of vesicles and the presence of smaller vesicles within larger ones was observed during the shear experiments. Structural heterogeneity is more pronounced in larger vesicles which have higher chances of collision and coalescence under flow due to their size. Smaller SMLVs, such as the ones in Figure 22c, look more ordered, with the bilayer structure extending up to the vesicle center (although a small pool could still be present). Once again, the radial

molecular arrangement is shown by the intensity pattern of the lamellar phase (bottom of Figure 22b). Overall, vesicles with radius in the range 50 – 150 μm show a large internal core while ones with radius in the range 5 – 20 μm have an extended structure of bilayers with a small core, if any. The absence of defects in smaller SMLVs is also shown by the presence of the Maltese cross (Figure 22d), which is indicative of a well ordered structure. This size-dependent difference in structure has an important consequence on vesicle flow behaviour. In fact, the larger SMLVs were deformed in the range of the shear rates investigated (0.1 – 10 s^{-1}) showing all the already mentioned dynamic regimes (i.e., tumbling, breathing, and tank-treading), while the smaller vesicles didn't show any deformation under flow but only a tumbling motion. A possible explanation of this difference is that the more compact and without defects internal structure of the smaller SMLVs doesn't allow their deformation.

The presence of structural heterogeneity and defects in larger SMLVs (Figure 22a) is likely to generate an excess area Δ , which can be considered as a mechanism underlying their flow-induced deformation. According to this hypothesis, SMLV deformation would be due to the unravelling of folded or re-entrant regions of the vesicle surface. In order to elucidate this point, vesicle shape at rest was investigated by confocal microscopy. In Figure 23 images of a vesicle from a typical z-stack and the corresponding 3D reconstruction by image analysis is presented together with three orthogonal projections.

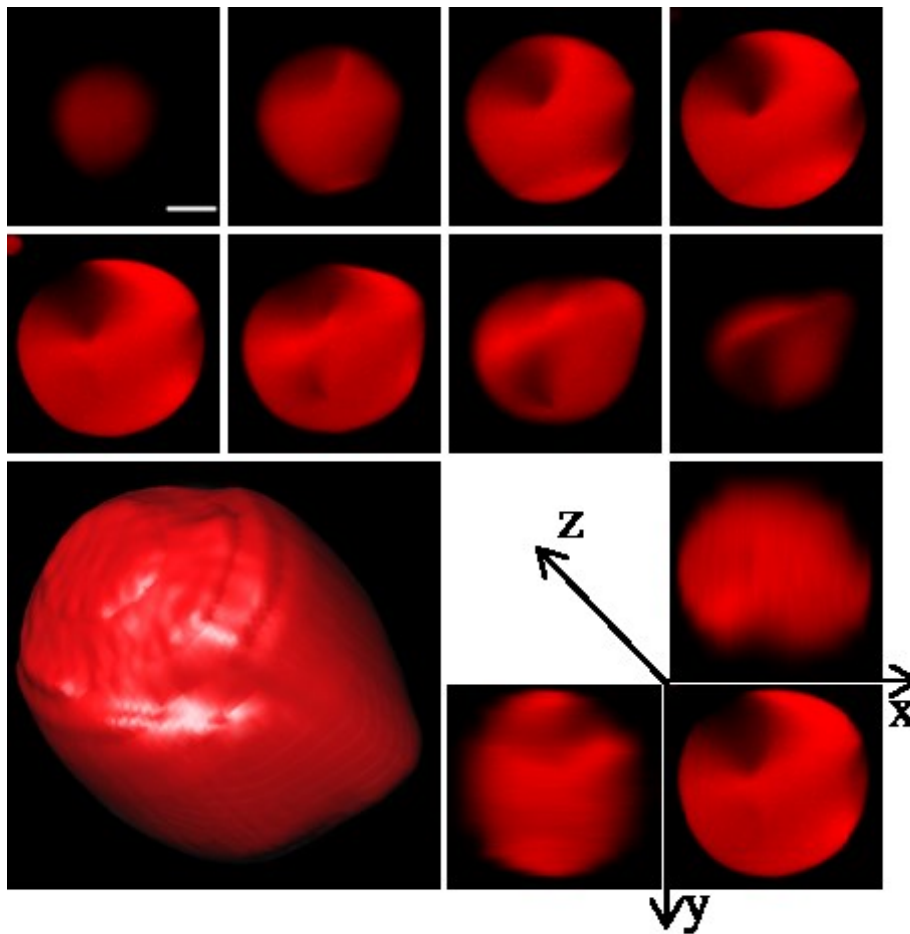


Figure 23. 3D reconstruction of a vesicle by confocal microscopy. Vesicle radius: 20 μm , number of z stack images: 10, objective: 40x/0.75 , scale bar = 10 μm .

The 3D rendering shows that vesicle shape is far from being spherical at rest, due to the presence of several surface and inner defects. The overall effect is to increase the actual surface area as compared to the one estimated by bright field microscopy, which is based on an apparent (quasi) spherical shape. A quantitative analysis of the 3D reconstruction provides both area A and volume of the vesicle. The resulting excess area $\Delta = (A - 4\pi R^2) / R^2$ is supposed to be an increasing function of the radius R , because of the higher number of defects found in larger vesicles (defect size ranges from 5 to 50

μm). In order to test this hypothesis, the relation between excess area and size of SMLVs was investigated. In Figure 24 Δ is plotted as a function of SMLV radius.

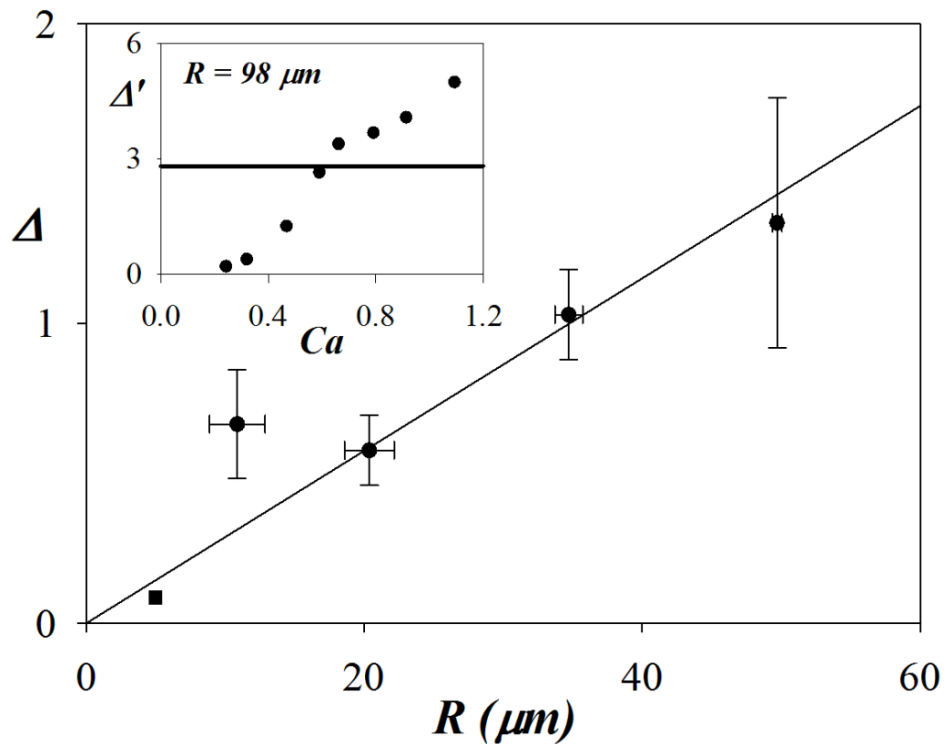


Figure 24. Plot of excess area vs vesicle radius (the error bars represent the standard deviations of the measurements). The continuous line is a linear fit to the data. As a reference, the excess area of a calibration microsphere ($R = 5 \mu\text{m}$) is also shown in the same plot as a square symbol. Δ' in the inset is the apparent excess area of a SMLV with $R = 98 \mu\text{m}$ calculated from the three vesicle axes.

The excess area was calculated by measuring the external surface SMLVs at rest by 3D image reconstruction. It can be seen that there is an increasing linear trend of the excess area with vesicle size of the SMLVs; this is due to the fact that larger SMLVs show a higher number of defects acting to increase their effective external surface. In the inset of Figure 24, the

apparent excess area Δ' of a vesicle is shown as a function of the capillary number Ca . The apparent excess area Δ' is calculated from the three axes a , b and c of the SMLV deformed under shear flow (i.e. $\Delta' = (A' - 4\pi R^2) / R^2$, where A' is the external area of an ellipsoid and is given by the approximate equation $A' = 4\pi[(a^p b^p + b^p c^p + a^p c^p)]^{1/p}$ with $p = 1.6075$). The three axes are measured by image analysis, as described in the experimental section. The so obtained apparent excess area Δ' is initially smaller than the excess area Δ (indicated by the continuous line) of the vesicle since, as long as the defects have not been completely unfolded by the action of flow, vesicle shape is not really ellipsoidal and the apparent surface obtained by the three axes is smaller than the actual one. At some point, when the surface is fully unfolded, Δ' becomes equal to Δ . At higher values of Ca , further vesicle deformation cannot be due to defects unfolding, but must be associated with the generation of new external surface and Δ' becomes greater than Δ .

In order to elucidate this mechanism of SMLV deformation, vesicles deformed by shear flow were observed under polarized light. A typical example is illustrated in Figure 25, where images of two SMLVs of comparable size are shown in both the velocity gradient and vorticity direction.

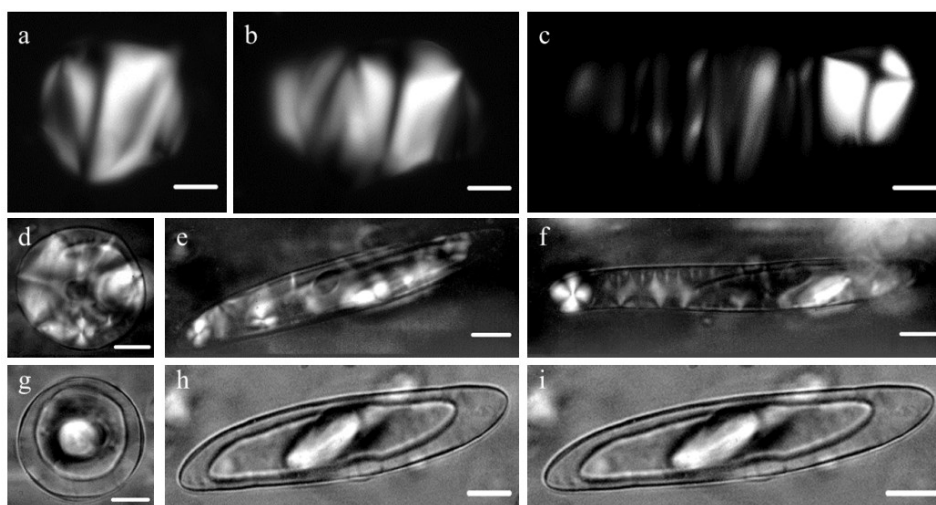


Figure 25. Images of sheared SMLVs. In the top sequence a SMLV is shown along the velocity gradient view under polarized light. In the other sequences a SMLV is shown along the vorticity view under polarized light (middle) and in bright field (bottom). Dimensional bar represents 50 μm .

In Figure 25a-c the shear-induced shape evolution is shown in the velocity gradient view under polarized light starting from the spherical shape at rest (Figure 25a) to a transient deformation (Figure 25b) until a steady state is reached (Figure 25c). The same sequence under polarized light is presented in Figure 25d-f for the view along the vorticity axis. In Figure 25g-i the shape evolution of the same SMLV of Figure 25d-f is shown along the vorticity axis in bright field.

The most striking feature of the deformed SMLV in Figure 25c is the presence of alternating bright and dark stripes on the surface when viewed along the velocity gradient. In the shear plane, conical structures are observed along the entire surface of the vesicle (apart from regions with core defects, which are due to the inclusion of smaller vesicles, e.g., the one with a Maltese cross on the far left side). These polarized light features are

typical of Parabolic Focal Conic (PFC) domains,⁸²⁻⁸⁴ a defect of a smectic A liquid crystal phase, which in this case is associated to the lamellar onion-like surfactant bilayers. These defects are generated when the parallel lamellar layers (represented by horizontal lines) are curved in conical domains following shear-induced undulation of the layers. A further evidence that the structures of Figure 25c and 22f correspond to PFC domains is provided by the image in Figure 26, where an extended lamellar region of the sample is observed under polarized light.

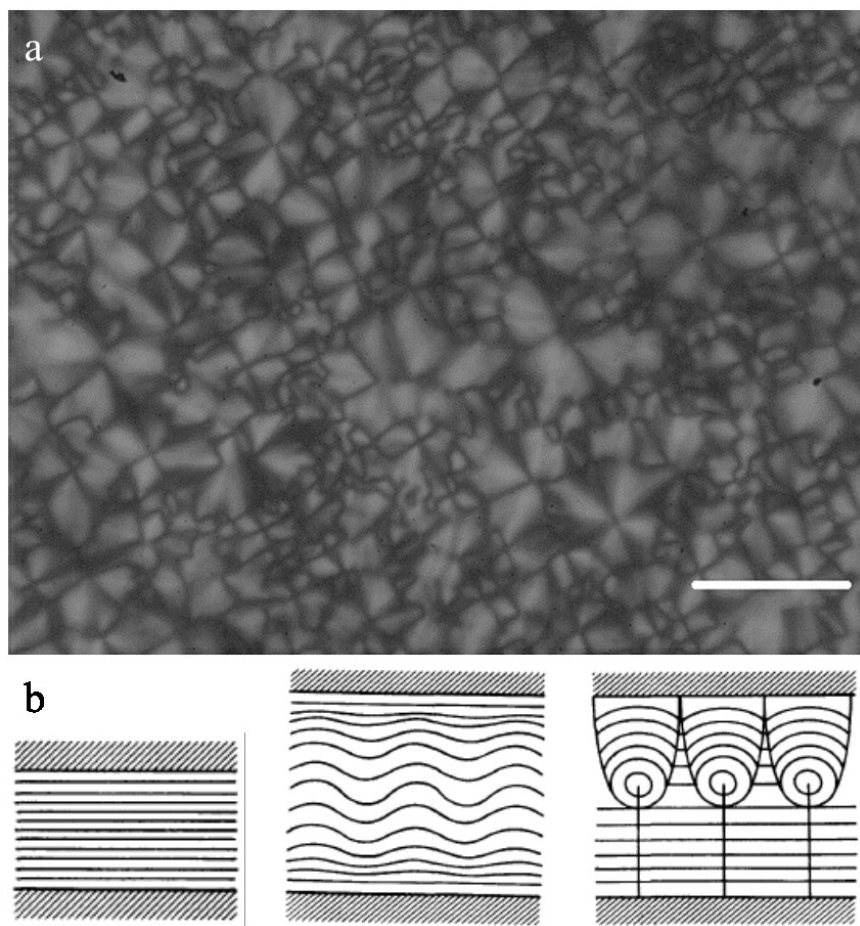


Figure 26. a) Non-ideal array of PFC domains in a lamellar region of the HLAS solution. Dimensional bar represents 50 μm . b) Formation of a Parabolic Focal Conic array in a homeotropic stacking due to a dilative stress (adapted from 83).

The polygonal texture of this region was found in other surfactant systems and is typical of PFC domains in the lamellar phase.⁸³

This mechanism of PFC domain generation has been already reported in the literature for smectic liquid crystals.^{85, 86} the idea is that the defects come from surface irregularities resulting from the dilation of the layers which generate local undulations (see the cartoons in Figure 26b). The latter are favoured because layer dilation comes with a much higher energetic cost than layer curvature.⁸⁷ A PFC defect consists of smectic layers around two singularity lines of parabolic shape,⁸⁷ as shown in the image of Figure 25f and schematically depicted in the cartoon of Figure 26b.

In smectic liquid crystals confined between parallel plates with homeotropic alignment (i.e., the director is perpendicular to the plate surface) layer undulation has to compete and can be suppressed by the anchoring condition. In our case, the SMLV outer shell is a free interface and this could help bilayer undulations thus promoting PFC formation. In addition, the shell undergoes a convection-induced re-arrangement with a thinning in the central region of the vesicle and the accumulation at the vesicle tips. This is due to the tank-treading motion at the interface and can be clearly seen in Figure 25g-i, where a vesicle is observed along the vorticity axis in bright field. By measuring the volume occupied by the shell from the images of Figure 25g-i, it is found that this re-arrangement occurs under constant shell volume.

4.1.4. Start-up and retraction

The mechanisms underlying shear-induced vesicle deformation can be also exploited (and further validated) by investigating SMLV transient behaviour. In Figure 27a the time-dependent trend of the deformation parameter of a SMLV having a radius of 70 μm under flow at a $\dot{\gamma} = 0.5 \text{ s}^{-1}$ is shown along the vorticity axis. It can be seen that when the flow is turned on the SMLV deforms reaching a steady state deformation after an initial damped oscillation. When the flow is turned off the SMLV retracts to its undeformed shape at rest. The oscillations of the deformation parameter during start-up show some analogy with the transient behaviour of emulsion droplets in the case $\lambda > 1$ predicted by Cox⁶⁷ and experimentally observed.⁶⁸ Based on this analogy, a comparison with Cox theory was made and is given by the continuous line in Figure 27a that represents the equation:⁶⁷

$$D_t = D \left[1 - 2 \exp\left(-\frac{20\dot{\gamma}t}{19Ca\lambda}\right) \cos(\dot{\gamma}t) + \exp\left(-\frac{40\dot{\gamma}t}{19Ca\lambda}\right) \right] \quad (5)$$

where D is the steady state value of D_t and t is the time.

Equation (5) was fit to the experimental results by using λ as the only fitting parameter and the calculations compare well with the initial part of the start-up data only (until D_t around 0.1), whereas the following oscillations are only qualitatively reproduced. A possible reason of this discrepancy is that Cox theory has been developed in the limit of small deformations, as already pointed out in the literature.⁶⁷

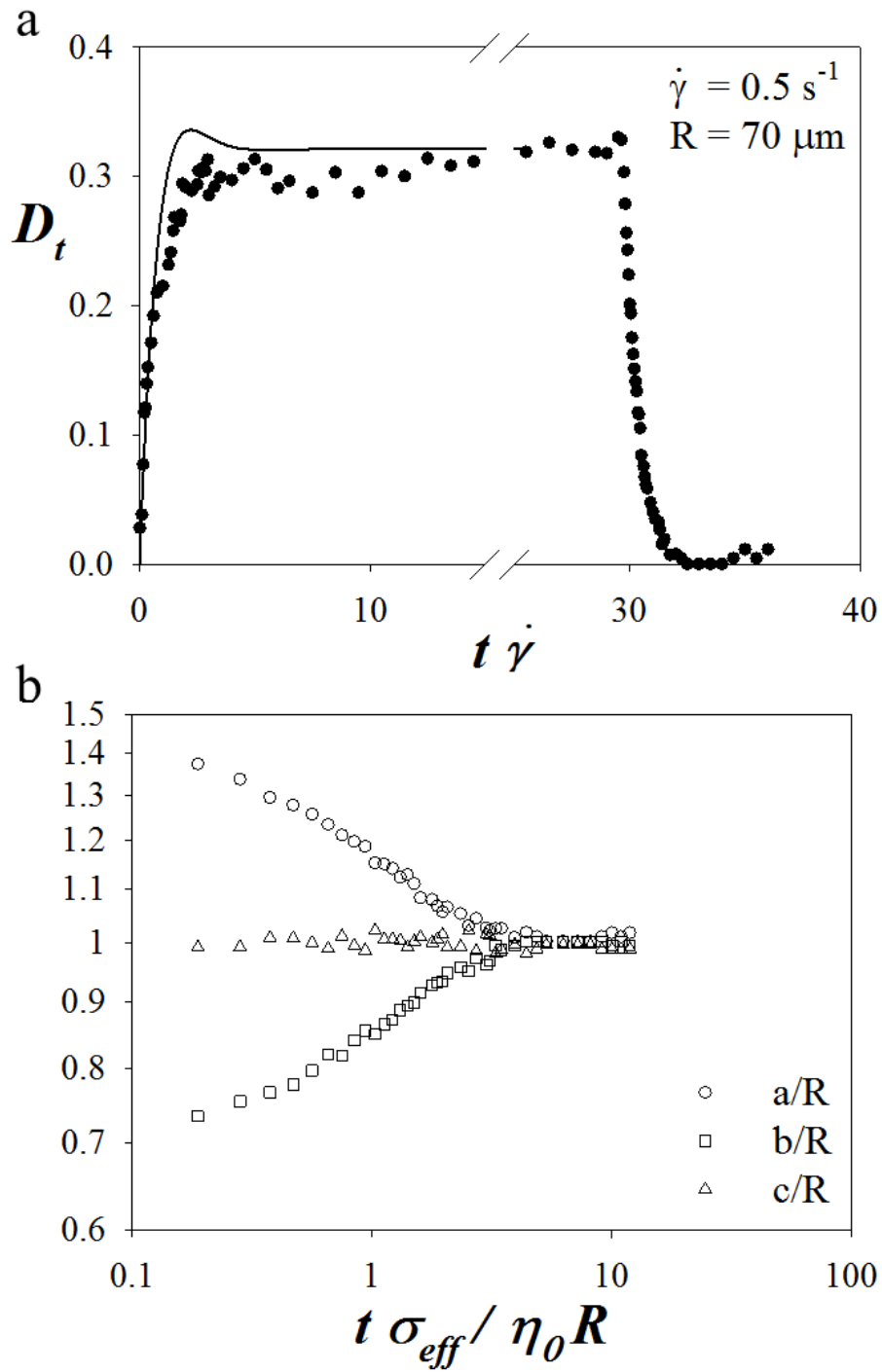


Figure 27. a) Transient behaviour of D for a SMLV undergoing tank-treading motion; b) Retraction of the three non-dimensional axes for the same SMLV.

The other transient deformation investigated in this study is vesicle retraction upon cessation of flow. An example is shown in Figure 27b where the relaxation of the three axis made non-dimensional with respect to the radius R (referred to the same SMLV of Figure 27a) is plotted as a function of time made non-dimensional by using the characteristic emulsion time $\eta_0 R / \sigma_{eff}$ ⁶⁹ with η_0 denoting the zero-shear viscosity of the sample (as mentioned previously, σ_{eff} was obtained from steady state deformation data and is equal to 10^{-4} N/m). The vesicle was observed along the vorticity axis and the third axis, c / R , was calculated by conservation of volume. As in droplet retraction, the three axis tend to recover the same value given by the undeformed vesicle radius at rest. However, some significant differences with respect to the droplet case can be noticed. First of all, while the two minor axes of a droplet collapse on the same curve during retraction,⁸⁸ the plot in Figure 27b shows that the three vesicle axes follow different paths of retraction, with the c axis remaining almost constant. In addition, another major difference between droplet and vesicle retraction is illustrated in Figure 28a, where the non-dimensional deformation parameter of several SMLVs is scaled according the following equation:⁶⁹

$$D_t = D \exp\left(-\frac{40(\lambda+1)}{(2\lambda+3)(19\lambda+16)} \frac{t\sigma_{eff}}{\eta_0 R}\right) \quad (13)$$

Equation (13) represents the scaling law of the retraction of the emulsion droplets according to the Rallison theoretical analysis (equation (6))⁶⁹ once σ_{eff} and η_0 were substituted with σ and η_c . The initial time ($t = 0$) of the retraction was chosen corresponding to a value of $D_0 = 0.15$ in order to stay

within the limits of the small deformation theory.⁶⁹ An inverse third power dependence on R , which is found in unilamellar vesicles, was then tested and the results are shown in Figure 28b for the same set of data as in Figure 28a.

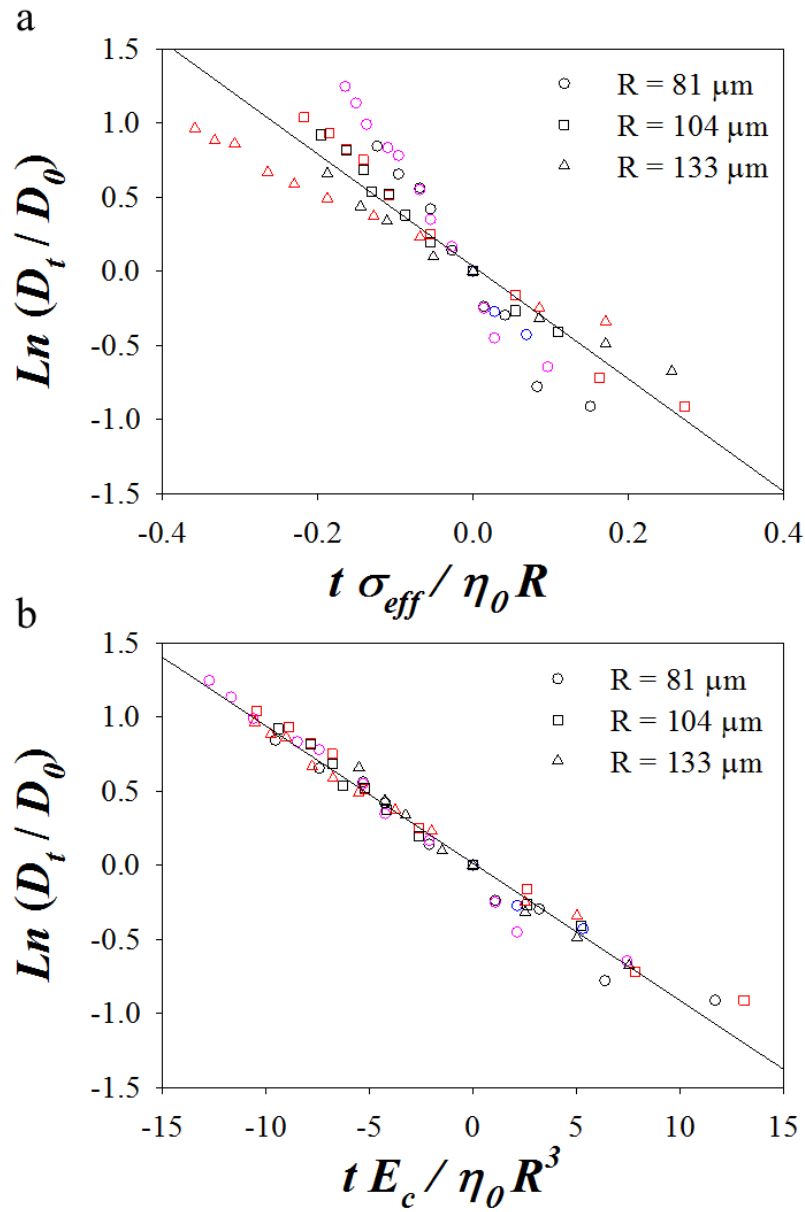


Figure 28. a) Plot of $\ln(D_t/D_0)$ vs the non-dimensional time ($t \sigma_{eff} / \eta_0 R$) during retraction of different SMLVs. b) Plot of $\ln(D_t/D_0)$ vs the non-dimensional time ($t E_c / \eta_0 R^3$) for same SMLVs.

A good scaling was found with non-dimensional time given by the expression $(t E_c / \eta_0 R^3)$, where the only fitting parameter E_c can be interpreted as the compressibility energy of the SLMV shell. A value of E_c equal to $5 \cdot 10^{-11}$ J was found from a linear fit, as shown by the continuous line in Figure 28b. By dividing E_c to the shell volume, which is almost the same for the vesicles in Figure 28 ($V_s \approx 2 \cdot 10^{-12}$ m³), a compressibility modulus B equal to 10 Pa is found, which is in agreement with literature data on lyotropic surfactant smectics.⁸⁹

4.2. Vesicle behaviour under capillary flow

In this chapter it is reported the analysis of the velocity and the deformation of the SMLVs under capillary flow. In Figure 29 it is shown the analysis of the velocity profiles of the three micro-capillaries used in the experiments. The experimental data were obtained by measuring the velocity of the SMLVs small enough to be considered as tracers and then a fitting of the data was done by using the following equation (10):

$$v = \frac{n}{n+1} \left(\frac{\Delta P}{2KL} \right)^{\frac{1}{n}} \left(R_t^{\frac{n+1}{n}} - r^{\frac{n+1}{n}} \right) \quad (10)$$

Equation (10) represents the velocity profile of a fluid with a power law viscosity under capillary flow and it was chosen due to the rheological behaviour of the HLAS sample shown in Figure 17.

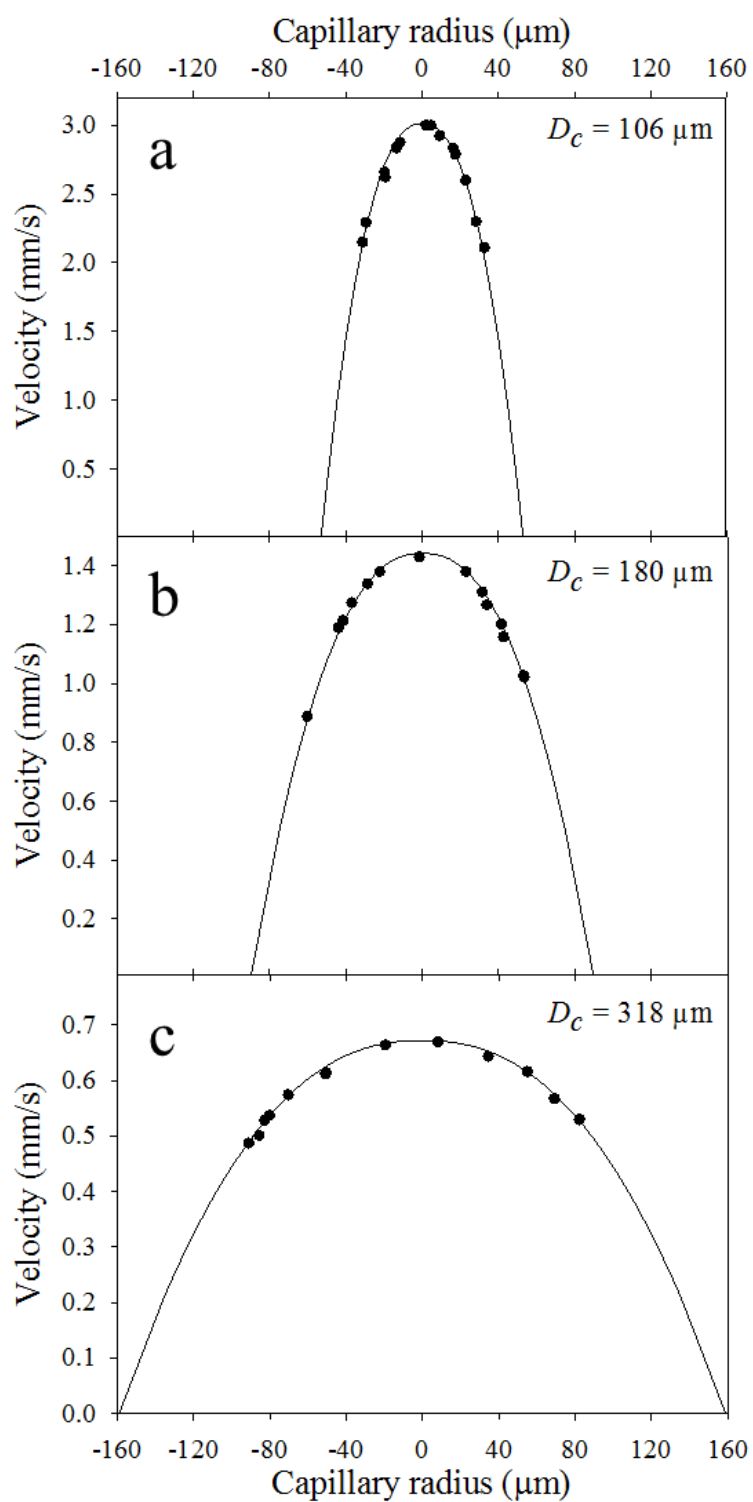


Figure 29. Velocity profiles of the HLAS samples in the three micro-capillary used.

The fitting of the data of Figure 29a gives a value of $n = 0.52$. The same value is obtained from the rheological data using the data corresponding at the same range ($0 - 1.5 \text{ s}^{-1}$) of the shear rates developed in the capillary flow (see Figure 30a). Similarly a value of n equals to 0.54 and 0.56 was obtained from the fitting of the data of Figure 29b and c respectively and the same agreement with the fitting of the rheological data was observed as well. In Figure 30 the shear rate profiles developed in the three micro-capillaries were shown. It can be seen the typical shear rate profile developed by a fluid undergoing capillary flow with the zero at the centre of the micro-capillary (i.e. $R_c = 0$) and the maximum value near the micro-capillary wall while the velocity profile is exactly the opposite with the maximum at the centre and the zero value at the wall. In Figure 30 it can be seen that the shear rate profiles in the three micro-capillaries are slightly different due to the different flow rate imposed and this is the reason of the difference in the fitting of the power law index n . In fact the fitting of the rheological data gives the same behaviour of n because of the two characteristic slopes shown in the shear viscosity profile (see Figure 17).

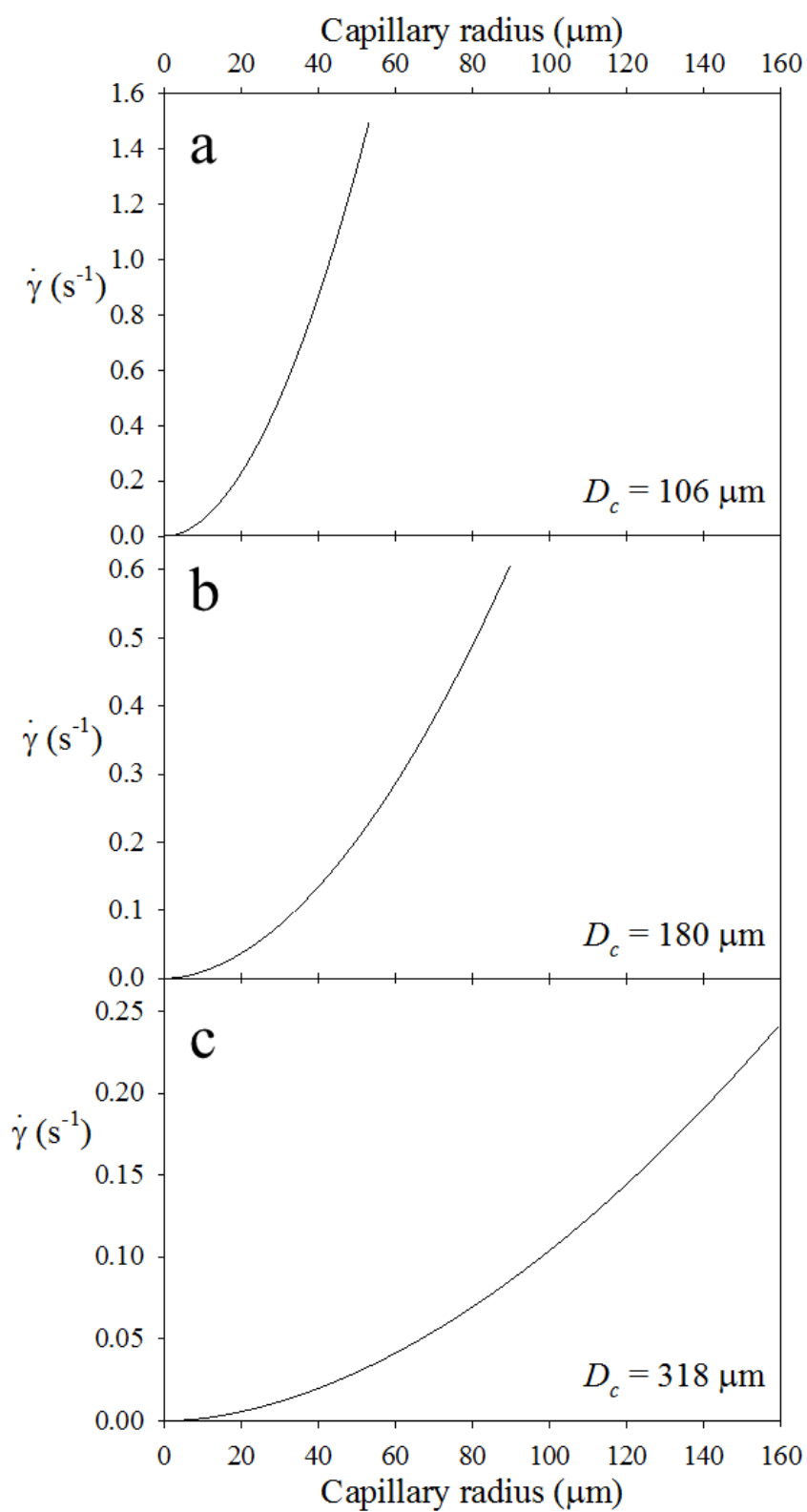


Figure 30. Shear rate profiles developed by the HLAS samples in the three micro-capillaries used.

In Figure 31 images of SMLVs deformed under capillary flow are shown. It can be seen the influence of the parameters Ca and k on the deformation. Indeed while at low capillary number or confinement degree the SMLVs show small deformations the increase of these parameters has the effect to deform more the vesicles. It is interesting to observe that the effect of k is more pronounced than the one of Ca ; a similar effect was also observed in the emulsion droplets under capillary flow where the confinement effect deform the drops more than the viscous stresses.

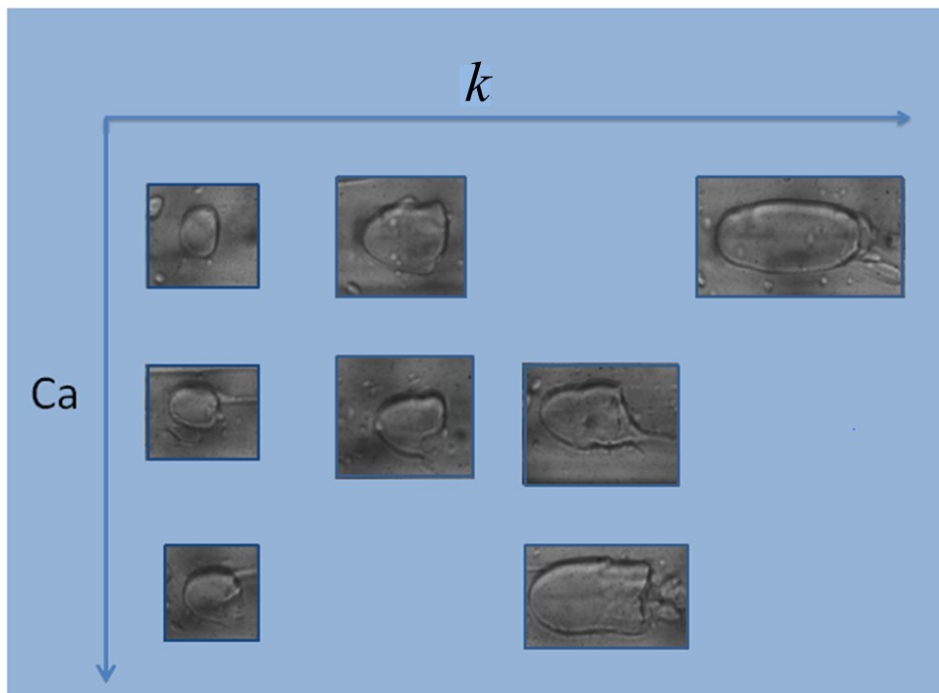


Figure 31. Images of deformed SMLVs under capillary flow.

A quantitative comparison between the behaviour of the SMLVs and the emulsion droplets under capillary flow was done by using the Hetsroni theory.⁷¹ In Figure 32 the trend of the velocity vs the confinement degree of several SMLVs is reported at several capillary number Ca .

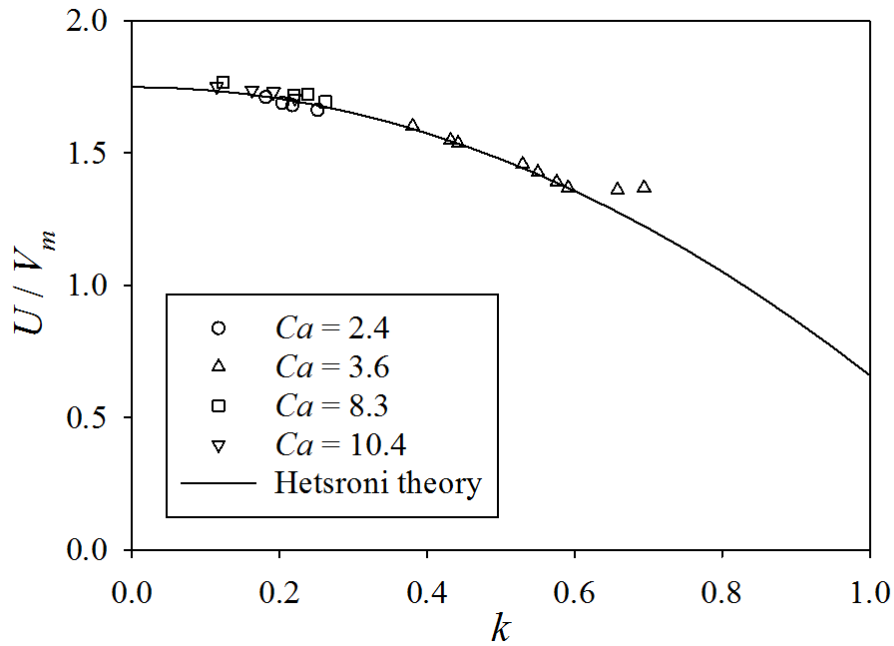


Figure 32. Scaling of the SMLV velocity with the confinement degree under capillary flow with $n = 0.59$. The continuous line is a fit of the data according to Hetsroni theory.

It can be seen that the ratio between the velocity U of the axial-symmetric SMLVs and the mean velocity V_m of several SMLVs at different Ca collapses on the same master curve showing a similar scaling with the emulsion droplets, especially at low values of confinement degree k . Instead at higher k values some experimental data put aside from the theoretical predictions showing the presence of a plateau. This behaviour was also observed in the emulsion droplets and is due to the fact that Hetsroni theory was developed for undeformed droplets (i.e. $Ca \rightarrow 0$ and $k \rightarrow 0$).

The continuous line of Figure 32 is a fit of the Hetsroni predictions where the only fitting parameter is the viscosity ratio λ . The so obtained value of λ , which is around 2, should be taken as an average quantity due to the shear

thinning of the surfactant solution viscosity. However it should be noticed that the value of λ is the same of that one obtained from the fitting of the deformation of the SMLVs under shear flow (see Figure 20).

It should be pointed out that Hetsroni theory was developed in Poiseuille flow conditions. Therefore in the following Hetsroni equation:⁷¹

$$\frac{U}{V_m} = 2 - \frac{4\lambda}{3\lambda+2} \cdot \kappa^2 + O(\lambda^3) \quad (12)$$

the term 2 representing the ratio between the maximum and the mean velocity in the Poiseuille flow need to be modified in order to be applied with HLAS solutions. In particular this term was changed in $\frac{1+3n}{1+n}$ that represents the same velocity ratio but in the case of a power law viscosity fluid. Therefore using a mean value of $n = 0.59$ a new velocity ratio of 1.75 was obtained and equation (12) becomes:

$$\frac{U}{V_m} = 1.75 - \frac{4\lambda}{3\lambda+2} \cdot \kappa^2 + O(\lambda^3) \quad (14)$$

and the equation (11) was used to fit the experimental data of Figure 32.

This SMLV dynamic behaviour under capillary flow does not change at different values of the power law index n . Indeed more experiments were performed at different flow rate obtaining a value of n equal to 0.51 and the Hetsroni theory still holds in this condition (see Figure 33) once the ratio between the maximum and the mean velocity was appropriately modified.

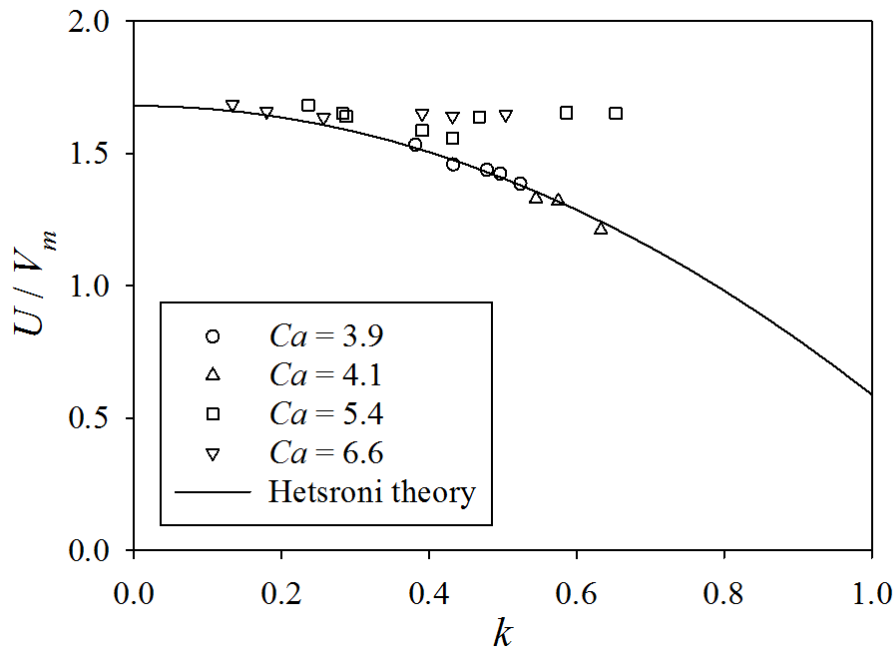


Figure 33. Scaling of the SMLV velocity with the confinement degree under capillary flow with $n = 0.51$. The continuous line is a fit of the data according to Hetsroni theory.

As before it can be seen the scaling of the different trends especially at low k values while at the highest Ca a deviation from the Hetsroni theory can be observed. Once again the continuous line is a fit of the experimental data according to Hetsroni theory⁷¹ where the only fitting parameter is the viscosity ratio λ and a value of c.a. 2 was obtained. This time the ratio between the maximum and the mean velocity of the equation (12) is 1.68 due to the different n value.

In Figure 34 it is shown how the SMLVs arrange themselves in the micro-capillary along the radial direction at different mean velocities V_m .

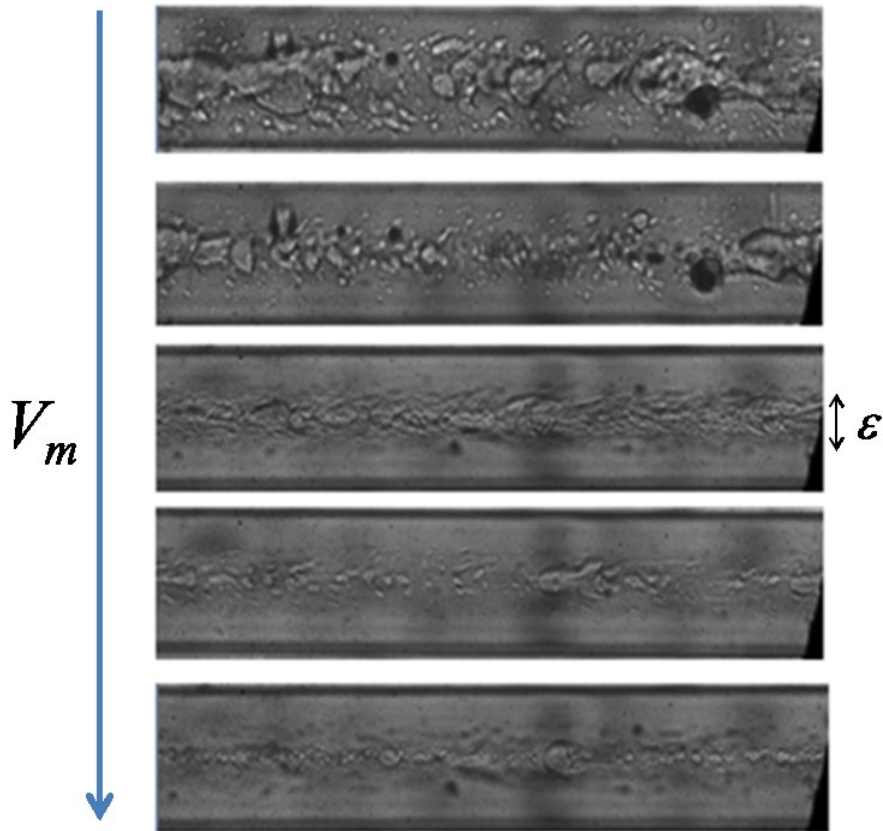


Figure 34. Decrease of the section ε at higher mean velocity V_m in a micro-capillary with a diameter of $180\ \mu\text{m}$.

It is interesting to observe that generally SMLVs occupy only the central section ε of the micro-capillary and not the entire available volume. Moreover, increasing V_m , this section becomes smaller up to occupy c.a. 30% of the available volume. This phenomenon was observed in all the three micro-capillaries utilized in the experiments and then a possible scaling of the phenomenon was investigated. In Figure 35 it is shown that the scaling of the data is achieved with the product between the mean velocity V_m and the micro-capillary diameter D_c . On the ordinate axis it is

reported the section ε made non-dimensional with the diameter D_c in order to make a comparison with different diameters.

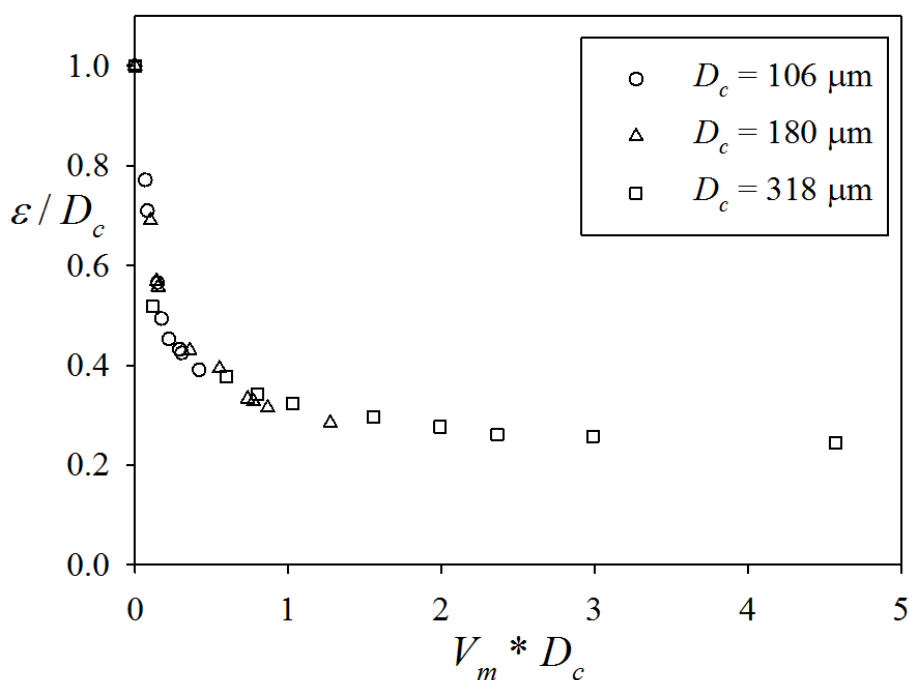


Figure 35. Scaling of the non-dimensional section ε .

4.3. Buchwald-Hartwig reaction

In this chapter we report on the use of a microreactor system to perform the Buchwald-Hartwig arylation using the newly developed **1** pre-catalyst (Figure 36, right side). In Figure 36, left side, the reaction is shown: an aryl bromide is coupled with a secondary amine in an organic solvent using **1** as pre-catalyst and a metal alkoxide as base to form an arylamine. The performance of the catalytic system in both batch and continuous flow is described and compared. The effects of residence time and temperature are studied in order to evaluate the influence of fluid dynamics on reactor

performance. Changes in tube diameter and solvent are also investigated.

Finally, a preliminary study of the reaction rate is shown.

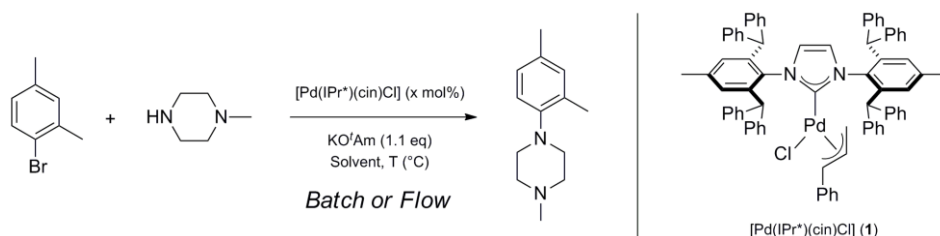


Figure 36. Left side: amination reaction; right side: the pre-catalyst $[Pd(IPr^*)(cin)Cl]$ (**1**).

4.3.1. Batch experiments

In Figure 37a, the conversion profiles are reported for several pre-catalyst concentrations in a batch reactor. It is shown, as expected, that an increase in catalyst loading allows higher conversions in shorter times. Indeed, the reaction reaches completion in only one minute for the highest palladium concentrations (0.5 - 1 mol%), in 10 minutes using 0.25 mol%, and finally in several hours at lower concentrations (0.12 - 0.16 mol%, 2 - 6h). These results exhibit once more the high catalytic activity of **1** in amination.⁶¹

Selectivity for the desired product was superior to 99% in all cases, as shown by the absence of any significant peaks apart from the ones of product and reagents in the chromatograms (data not shown for the sake of brevity).

In Figure 37b, the initial rates of the reaction are shown for different amine concentrations. The reaction kinetics does not change with varied amounts of amine, there is apparently a zero-order dependence of the amine

concentration on the reaction rate. The same dependence has been found for the Buchwald-Hartwig amination catalysed by Pd-BINAP system, cfr. equation (1).⁵⁰

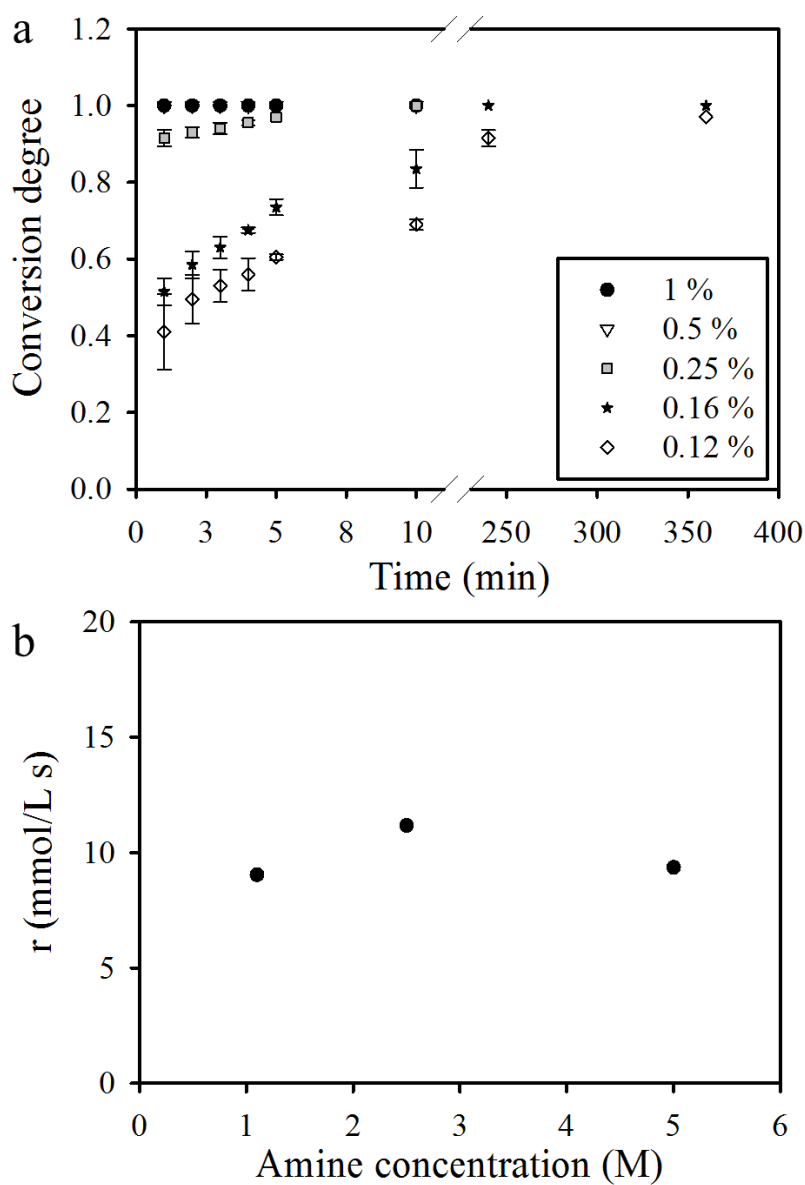


Figure 37. a) Conversion profiles for several molar ratios of pre-catalyst loading at 50°C with an initial concentration of 1 M of ArBr, 1.1 M of amine, 1.1 M of base, 0.13 M of decane as internal standard, DME (1 mL); b) Initial reaction rates for different amine concentrations in the presence of 0.12% of pre-catalyst.

4.3.2. Continuous flow experiments

In Figure 38a, the conversion profiles are shown for several pre-catalyst concentrations in the microreactor. It can be seen that increasing the catalyst loading allows better performance under flow as well. At the highest catalyst loadings (1 – 0.25 mol%), the reaction is complete with very short residence times (1 – 10 min). Selectivity for the desired product was better than 99% in all cases, as evaluated by product yields. The initial reaction rates for different pre-catalyst concentrations are reported in Figure 38b for the different values of pre-catalyst concentration. As shown in Figure 38b data are well represented by a second-order kinetics in the pre-catalyst concentration, as follows:

$$r = [Cat]^2$$

where $[Cat]$ is the pre-catalyst concentration. This dependence is different compared to equation (1) where the $[Pd(BINAP)]$ system shows a linear first-order dependence on the palladium concentration and a reciprocal first-order dependence on ligand concentration.

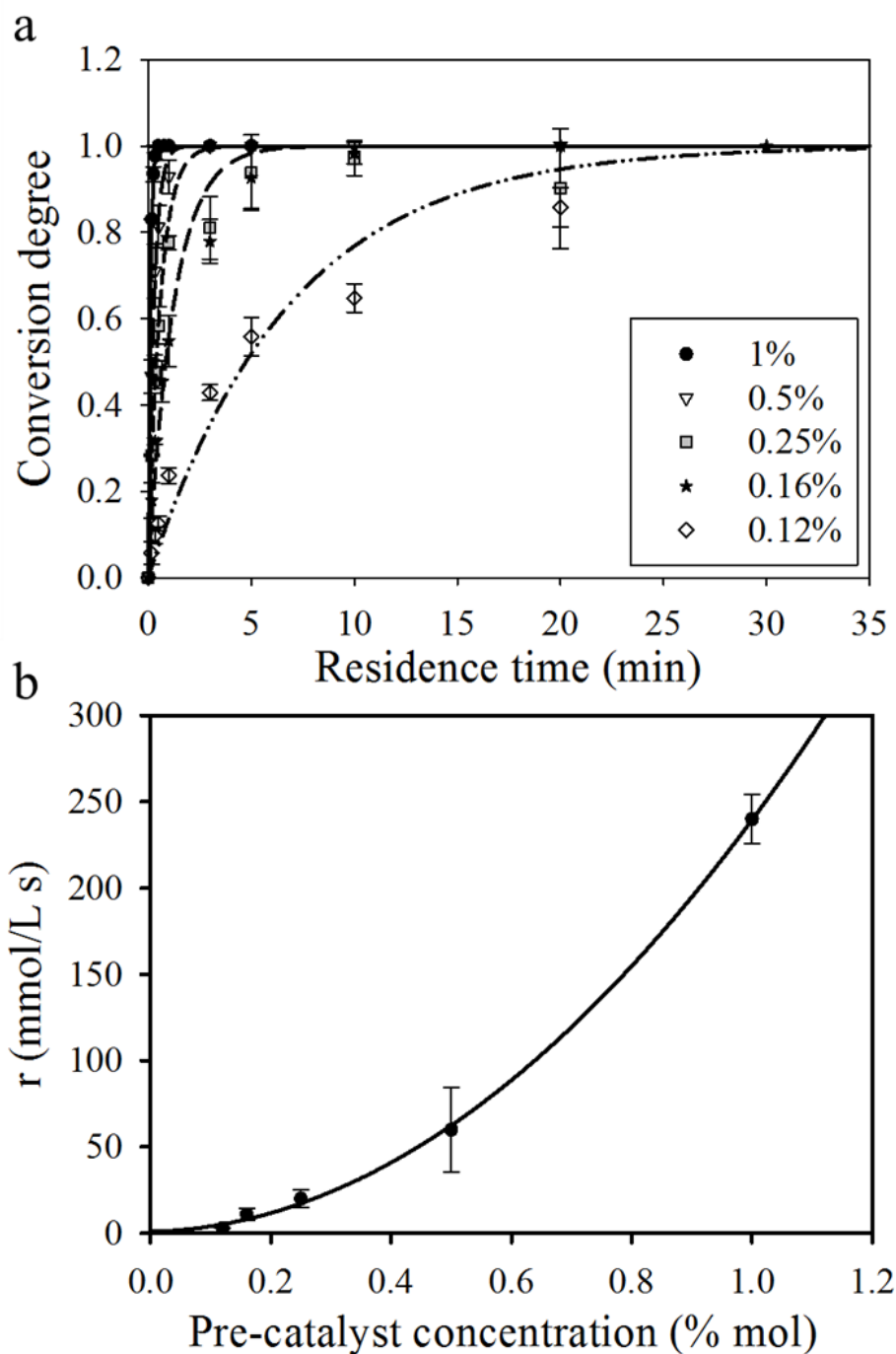


Figure 38. a) Conversion profiles for different catalyst loading at 50°C with an initial concentration of 0.11 M of ArBr, 0.12 M of amine, 0.12 M of base, 3.7 mM of 4,4'-di-tert-butylbiphenyl as internal standard, DME (18 mL). The continuous lines are exponential fitting of the data. Microreactor with 1 mm i.d. has been used; b) Initial reaction rates for different pre-catalyst concentrations.

The dependence of the reaction kinetics on the halide concentration was also investigated. In Figure 39, the reaction rate is plotted as a function of ArBr concentration and a linear dependence is found. The latter is consistent with the exponential fitting shown in Figure 38a.

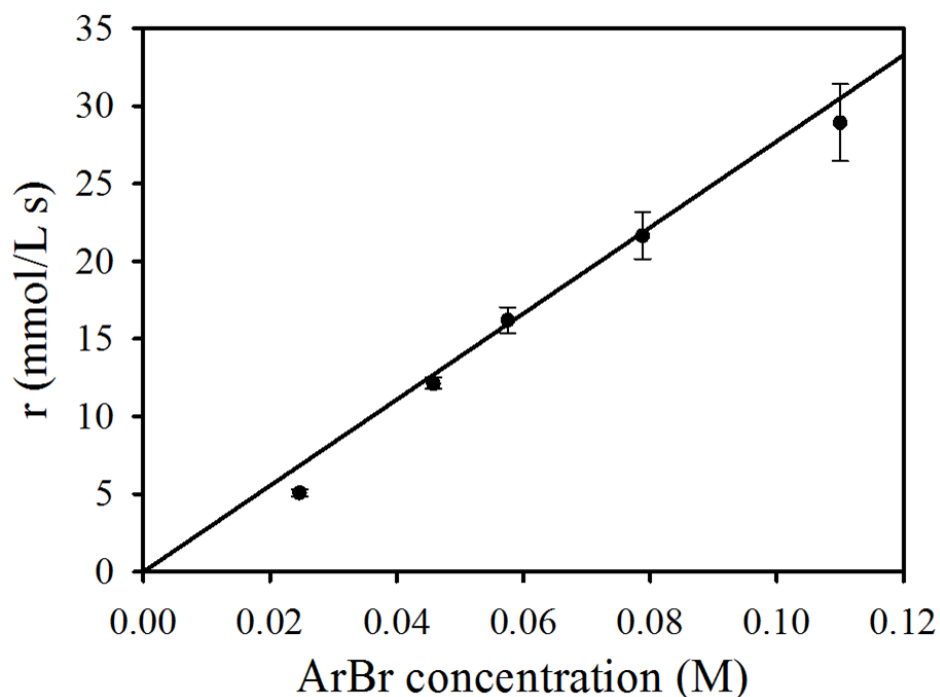


Figure 39. Initial reaction rates for different halide concentrations with a 0.25% of pre-catalyst.

Indeed, an exponential rise of the conversion with time is equivalent to a linear dependence of the reaction rate on reagents concentration and, in particular, on ArBr concentration because of the zero-order dependence of kinetics on the amine previously shown in Figure 37b.

Overall, the reaction kinetics appears to obey the following equation:

$$r = k_t [Cat]^2 [ArBr] \quad (15)$$

where $[Cat]$ and $[ArBr]$ are the pre-catalyst and aryl bromide concentrations, respectively, and k_t is a temperature-dependent kinetic constant. Equation (15), though obtained from a preliminary data analysis, provides, to our knowledge, the first expression in the literature of the amination reaction rate when using a $[Pd(NHC)]$ pre-catalyst. Further investigations, notably on the temperature dependence of the kinetic constant and to further support the pre-catalyst concentration dependence, are currently being explored in our laboratories.

One of the differences between batch and continuous flow reactions is the dilution of the reaction medium. In batch, the reaction medium is highly concentrated (1 M of ArBr) to induce fast reactivity. In flow, a lower concentration of the reagents (0.11 M of ArBr) is used in order to reduce the amounts of insoluble potassium bromide salt (KBr) produced by the reaction and consequently avoid clogging of the microreactor. We were then interested to compare the reactivity of the system at the same concentration (0.11 M ArBr) in both batch and flow operation. Such comparison is shown in Figure 39 where conversion is plotted as a function of time.

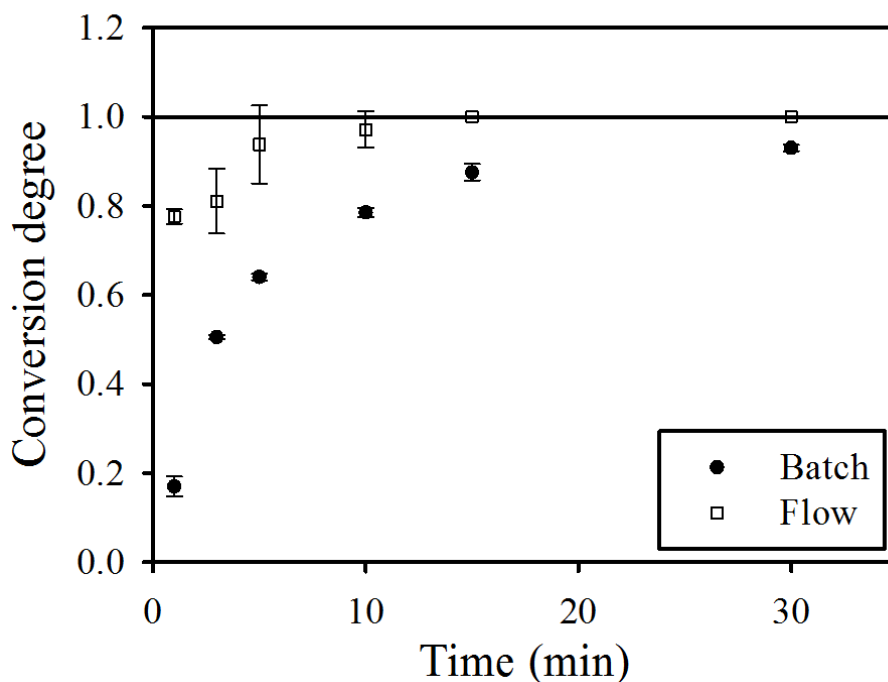


Figure 40. Comparison between batch and continuous flow microreactor operation at 50°C with the following initial concentrations: 0.11 M of ArBr, 0.12 M of amine, 0.12 M of base, 0.25 mol% of **1**, 3.7 mM or 0.13 M of internal standard, DME (9 mL). Microreactor with 1 mm i.d. was used.

The two sets of data in Figure 40 show a faster reactivity in flow than in batch operation. Indeed, the completion of the reaction in flow was observed with a time of 10 min at a palladium concentration of 0.25 mol%. On the other hand, in batch, 30 min were required to reach complete conversion. The better performance of the continuous flow microreactor can generally be explained in terms of two enhanced transport phenomena: mass transfer or heat exchange. In our case, the reaction is initially homogeneous, and as a consequence, mass transfer should not play a significant role. A more efficient heat exchange in the microreactor because of its larger surface to volume ratio appears then as the right explanation. Faster heat exchange

improving the kinetics of the Buchwald-Hartwig amination at low catalyst loading has already been reported in the literature, when heating of the reactor is performed by using microwaves rather than thermostatic baths.⁹⁰ In this study, it was suggested that the phenomenon was related to the presence of a short lifetime effective catalyst generated in situ. The presence of a better heat exchange may minimize a catalyst decomposition pathway, allowing faster conversion, especially during the initial reaction burst. Hence, the difference between batch and continuous flow is expected to appreciably decrease by working at higher catalyst loading, because catalyst decomposition becomes less significant.

In Figure 41, the influence of the temperature on the continuous flow reaction is reported. An increase in bath temperature leads to a faster reaction kinetics. From an industrial point of view, although it is likely that no substantial benefit is provided by going from 30° to 50° C in terms of heating costs, the corresponding increase of reactivity would allow one to obtain higher conversions with smaller amounts of catalyst (which is the most expensive component in the B-H reaction), thus contributing to optimize processing conditions. Of course, the increase of temperature would be limited by the boiling point of the solvent, above which the microreactor should be operated under pressure, thus making the system economically disadvantageous.

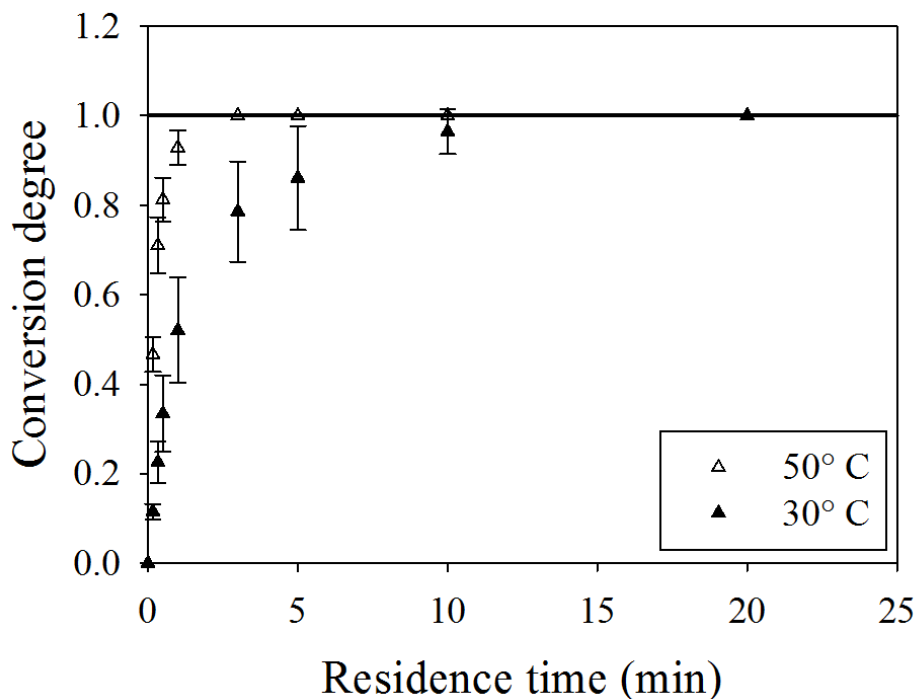


Figure 41. Comparison of the conversion profiles at two different temperatures with the following initial concentrations: 0.11 M of ArBr, 0.12 M of amine, 0.12 M of base, 0.5 mol% of **1**, 3.7 mM of internal standard, DME (18 mL). Microreactor with 1 mm i.d. was used.

In Figure 42, the influence of the microreactor internal diameter and of the solvent on the kinetics of the reaction is shown. Concerning the former (Figure 42a), no change in conversion was found by using either 1 mm or 2 mm i.d. tubings. Once again, this result can be explained by the fact that heat transfer resistance is quite low and comparable in both cases. Concerning the solvents (Figure 42b), a 2 mm ID microreactor was used to compare toluene and DME. This choice is due to the fact that by using a 1 mm ID microreactor with toluene, clogging of the microreactor was observed. It is to be noted that no clogging was previously observed by using DME. This could be explained by the different solubility of KBr in

both solvents. KBr is a poorly soluble salt in organic solvents. It nucleates and precipitates more rapidly in the less polar solvent, in this case toluene, thus leading to microreactor clogging. However, KBr precipitation is not fast enough in DME to block the microreactor. A better microreactor performance was found in DME, yielding complete conversion within one minute. On the other hand, a residence time of 30 minutes was needed to reach completion in toluene. This result is in agreement with batch experiments, which show that the reaction is faster in DME than in toluene due to the stabilising effect of the solvent on the palladium active catalyst.

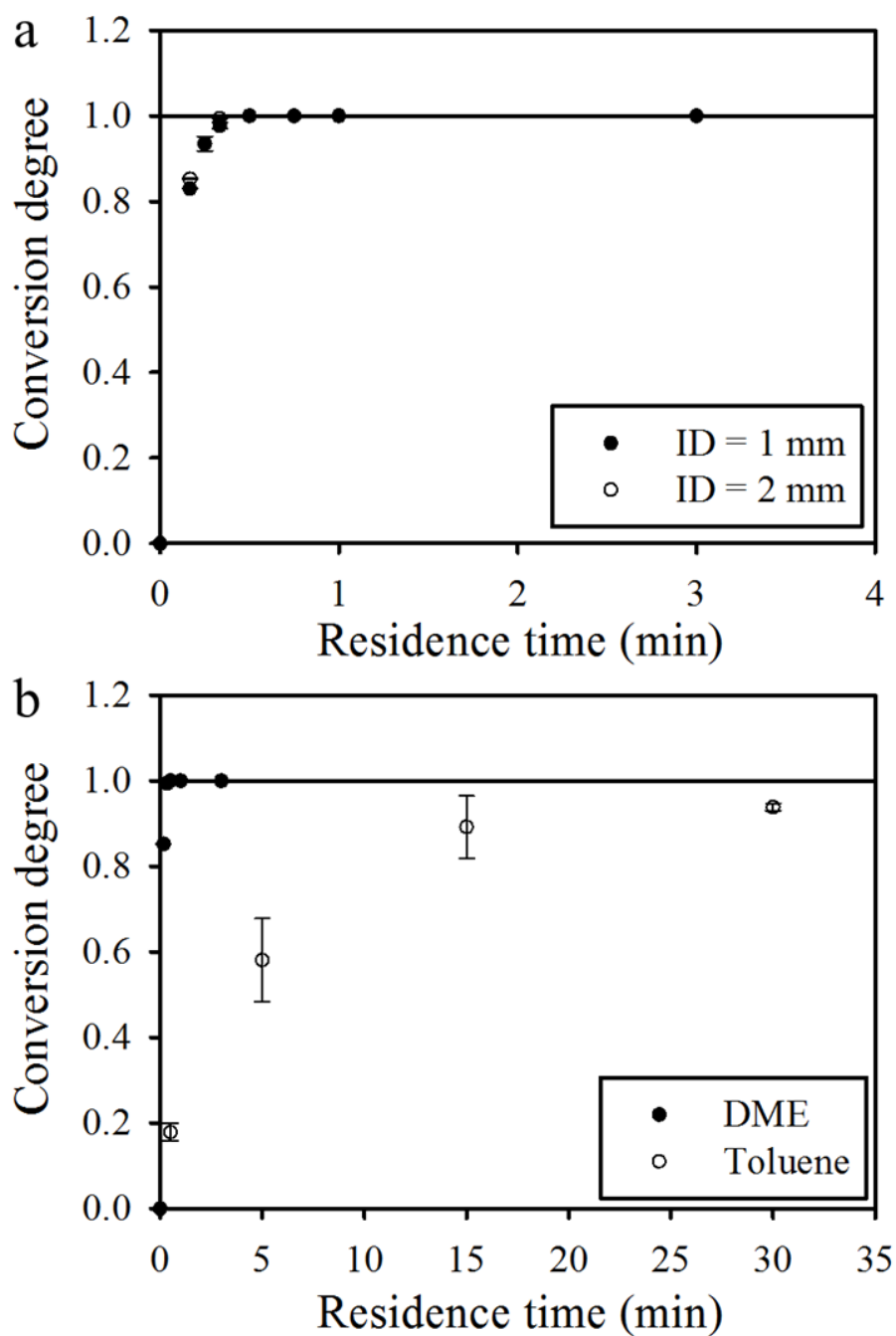


Figure 42. a) Comparison between two different internal diameters of the microreactor at 50°C. Initial concentrations are 0.11 M of ArBr, 0.12 M of amine, 0.12 M of base, 1 mol% of **1**, 3.7 mM of internal standard, DME (18 mL); b) Comparison between two different solvents at 50°C. DME case: 0.11 M of ArBr, 0.12 M of amine, 0.12 M of base, 1 mol% of **1**, 3.7 mM of internal standard, DME (18 mL). Toluene case: 0.11 M of ArBr, 0.12 M of amine, 0.12 M of base, 1 mol% of **1**, 3.7 mM of internal standard, toluene (18 mL). Microreactor with 2 mm i.d. has been used.

5. Conclusions

In conclusion, an investigation of the dynamic behaviour of the SMLVs of a commercial surfactant has been carried out under shear and capillary flow. Under shear flow it was seen that the deformation parameter of SMLVs scales with R (instead of R^3 as for unilamellar vesicles) and a nonzero value of the effective interfacial tension is measured. These features, together with volume preservation, are in analogy with sheared emulsion droplets at viscosity ratio $\lambda > 1$ and elastic capsules. The mechanism governing the deformation of the SMLVs under flow has been shown. Their deformation is made possible by the presence of both the excess area and the defect generation of the external surface allowing the SMLVs to reach high values of deformation. Only the bigger SMLVs showing a large internal core have been seen to deform while the smaller ones do not deform in our experimental conditions because of their compact and well-structured bilayer disposition. The retraction of the SMLVs is governed especially by the bending stresses of the lamellae rather than the surface tension which is the predominant stress in the flow induced deformation.

Under capillary flow it was confirmed that the HLAS solution can be considered as a power law viscosity fluid by the analysis of the velocity profiles in agreement with rheological data. Afterwards another analogy in the dynamic behaviour between the SMLVs and the emulsion droplets under capillary flow was shown by using the Hetsroni theory. Finally the SMLVs were seen to concentrate themselves only in the central section of

the micro-capillaries especially at the highest velocity. This phenomenon was observed in different micro-capillaries and a scaling with the product between the velocity and the micro-capillary diameter using different diameters.

The present study shows the complex behaviour of the SMLVs under flow and the results of this work are relevant in the processing of surfactant based systems, where the final product properties are dependent on the presence of the flow-generated SMLVs.

An example of this kind of industrial applications is the Buchwald-Hartwig amination where the surfactants are used in the multiphasic systems. Regarding this reaction a continuous flow microreactor has been developed for the homogeneous Buchwald-Hartwig aryl amination reaction, by using a well-defined palladium-NHC complex. A comparison between batch and continuous flow reactions was presented and it was shown that the B-H reaction is faster in the microreactor than in batch. The improvement is more significant at the lowest catalyst loadings, most likely because of the better heat transfer provided by the microreactor. This is due to the smaller surface to volume ratio of the latter. Additionally, an investigation of the influence of the microreactor operational parameters on the reaction system was carried out. An increase in the reaction temperature allows a faster conversion simply due to faster kinetics. Moreover, the use of a microreactor with smaller inner diameter shows better performance. The role of the solvent was investigated, by examining two organic solvents,

toluene and DME. DME was found to allow a faster conversion and avoids clogging in the microreactor. Finally, the dependence of reagent and pre-catalyst concentrations have been delineated. The rate expression shown in equation (7) shows a zero-order dependence on the amine concentration and a first-order dependence on the aryl bromide concentration. For the pre-catalyst, a second-order dependence has been found.

The results of this successful application of the B-H reaction in a continuous flow microreactor can be considered relevant in the processing of pharmaceutical industry, where an increase of the productivity is constantly pursued always maintaining very high the purity of the product and then the selectivity of the process.

6. Bibliography

1. K. Holmberg, B. Jönsson, B. Kronberg and B. Lindman, *Surfactants and Polymers in Aqueous Solution*, Wiley, 2002.
2. T. F. Tadros, *Applied Surfactants*, Wiley, 2006.
3. V. Guida, *Advances in Colloid and Interface Science*, 2010, **161**, 77-88.
4. J. N. Israelachvili, *Intermolecular and Surface Forces: Revised Third Edition*, Academic Press, 2011.
5. K. L. Mittal and B. Lindman, *Surfactants in Solution*, Springer, 1999.
6. M. J. Rosen and J. T. Kunjappu, *Surfactants and Interfacial Phenomena*, Wiley, 2012.
7. J. Li, M. Zhao and L. Zheng, 2012, **396**, 16-21.
8. M. G. Berni, C. J. Lawrence and D. Machin, *Advances in Colloid and Interface Science*, 2002, **98**, 217-243.
9. H. Noguchi and G. Gompper, *Physical Review Letters*, 2004, **93**, 258102.
10. V. V. Lebedev, K. S. Turitsyn and S. S. Vergeles, *Physical Review Letters*, 2007, **99**, 218101.
11. C. Misbah, *Physical Review Letters*, 2006, **96**, 028104.
12. W. Helfrich, *Journal of Physics: Condensed Matter*, 1994, **6**, A79.
13. N. J. Zabusky, E. Segre, J. Deschamps, V. Kantsler and V. Steinberg, *Physics of Fluids*, 2011, **23**, 041905.

14. O. Diat, D. Roux and F. Nallet, *Journal De Physique Ii*, 1993, **3**, 1427-1452.
15. O. Diat and D. Roux, *Journal De Physique Ii*, 1993, **3**, 9-14.
16. M. Kepczynski, J. Bednar, D. Kuźmich, P. Wydro and M. Nowakowska, *Langmuir*, 2010, **26**, 1551-1556.
17. H. Hoffmann, C. Thunig, P. Schmiedel and U. Munkert, *Langmuir*, 1994, **10**, 3972-3981.
18. K. Tsuchiya, H. Nakanishi, H. Sakai and M. Abe, *Langmuir*, 2004, **20**, 2117-2122.
19. F. M. Menger, S. J. Lee and J. S. Keiper, *Langmuir*, 1996, **12**, 4479-4480.
20. S. J. Singer and G. L. Nicolson, *Science*, 1972, **175**, 720-731.
21. C. M. Paleos, D. Tsiourvas and Z. Sideratou, *Langmuir*, 2011, **28**, 2337-2346.
22. K. R. Rosholm, A. Arouri, P. L. Hansen, A. González-Pérez and O. G. Mouritsen, *Langmuir*, 2011, **28**, 2773-2781.
23. S. Mann, J. P. Hannington and R. J. P. Williams, *Nature*, 1986, **324**, 565-567.
24. R. A. Moss and G. O. Bizziogetti, *Journal of the American Chemical Society*, 1981, **103**, 6512-6514.
25. I. I. Yaacob, A. C. Nunes, A. Bose and D. O. Shah, 1994, **168**, 289-301.

26. G. I. Taylor, *Proceedings of the Royal Society of London. Series A*, 1934, **146**, 501-523.
27. B. Medronho, S. Shafaei, R. Szopko, M. G. Miguel, U. Olsson and C. Schmidt, *Langmuir*, 2008, **24**, 6480-6486.
28. B. Medronho, S. Fujii, W. Richtering, M. G. Miguel and U. Olsson, *Colloid and Polymer Science*, 2005, **284**, 317-321.
29. S. Koschoreck, S. Fujii and W. Richtering, *Progress of Theoretical Physics*, 2008, 154-165.
30. E. Vanderlinden and J. H. M. Droge, *Physica A*, 1993, **193**, 439-447.
31. M. Richterova and V. Lisy, *General Physiology and Biophysics*, 2005, **24**, 89-97.
32. I. Koleva and H. Rehage, *Soft Matter*, 2012, **8**, 3681-3693.
33. A. Kirschning, *Beilstein Journal of Organic Chemistry*, 2009, **5**, No. 15.
34. Y. Takebayashi, K. Sue, S. Yoda, T. Furuya and K. Mae, *Chemical Engineering Journal*, 2012, **180**, 250-254.
35. C. B. Kelly, C. Lee, M. A. Mercadante and N. E. Leadbeater, *Organic Process Research & Development*, 2011, **15**, 717-720.
36. G. M. Whitesides, *Nature*, 2006, **442**, 368-373.
37. E. V. Rebrov, J. C. Schouten and M. H. J. M. de Croon, *Chemical Engineering Science*, 2011, **66**, 1374-1393.
38. V. Kumar, M. Paraschivoiu and K. D. P. Nigam, *Chemical Engineering Science*, 2011, **66**, 1329-1373.

39. T. Noel and S. L. Buchwald, *Chemical Society Reviews*, 2011, **40**, 5010-5029.
40. S. Kotha, K. Lahiri and D. Kashinath, *Tetrahedron*, 2002, **58**, 9633-9695.
41. K. L. Billingsley, K. W. Anderson and S. L. Buchwald, *Angew. Chem. Int. Ed.*, 2006, **45**, 3484-3488.
42. A. F. Littke, C. Dai and G. C. Fu, *Journal of the American Chemical Society*, 2000, **122**, 4020-4028.
43. J. F. Hartwig, in *Handbook of Organopalladium Chemistry for Organic Synthesis*, ed. J. W. Sons, New York, Editon edn., 2003.
44. A. R. Muci and S. L. Buchwald, in *Cross-Coupling Reactions*, ed. N. Miyaura, Springer Berlin Heidelberg, Editon edn., 2002.
45. L. Jiang and S. L. Buchwald, in *Metal-Catalyzed Cross-Coupling Reactions*, eds. A. Meijere and F. Diederich, Wiley-VCH, Weinheim, Editon edn., 2004.
46. J. F. Hartwig, *Accounts of Chemical Research*, 2008, **41**, 1534-1544.
47. M. Kosugi, M. Kameyama and T. Migita, *Chem. Lett.*, 1983, **12**, 927-928.
48. A. S. Guram, R. A. Rennels and S. L. Buchwald, *Angewandte Chemie International Edition in English*, 1995, **34**, 1348-1350.
49. J. Louie and J. F. Hartwig, *Tetrahedron Letters*, 1995, **36**, 3609-3612.

50. S. Shekhar, P. Ryberg, J. F. Hartwig, J. S. Mathew, D. G. Blackmond, E. R. Strieter and S. L. Buchwald, *Journal of the American Chemical Society*, 2006, **128**, 3584-3591.
51. D. S. Surry and S. L. Buchwald, *Chemical Science*, 2011, **2**, 27-50.
52. A. F. Littke and G. C. Fu, *Angewandte Chemie International Edition*, 2002, **41**, 4176-4211.
53. M. S. Viciu, R. M. Kissling, E. D. Stevens and S. P. Nolan, *Organic Letters*, 2002, **4**, 2229-2231.
54. N. Marion, E. C. Ecarnot, O. Navarro, D. Amoroso, A. Bell and S. P. Nolan, *Journal of Organic Chemistry*, 2006, **71**, 3816-3821.
55. N. Marion, O. Navarro, J. Mei, E. D. Stevens, N. M. Scott and S. P. Nolan, *J. Am. Chem. Soc.*, 2006, **128**, 4101-4111.
56. N. Marion and S. P. Nolan, *Accounts of Chemical Research*, 2008, **41**, 1440-1449.
57. M. G. Organ, M. Abdel-Hadi, S. Avola, I. Dubovyk, N. Hadei, E. A. B. Kantchev, C. J. O'Brien, M. Sayah and C. Valente, *Chem.--Eur. J.*, 2008, **14**, 2443-2452.
58. Z. Jin, S.-X. Guo, X.-P. Gu, L.-L. Qiu, H.-B. Song and J.-X. Fang, *Advanced Synthesis & Catalysis*, 2009, **351**, 1575-1585.
59. G. C. Fortman and S. P. Nolan, *Chemical Society Reviews*, 2011, **40**, 5151-5169.
60. A. Chartoire, M. Lesieur, L. Falivene, A. M. Z. Slawin, L. Cavallo, C. S. J. Cazin and S. P. Nolan, *Chem.--Eur. J.*, 2012, **18**, 4517-4521.

61. A. Chartoire, X. Frogneux and S. P. Nolan, *Adv. Synth. Catal.*, 2012, **354**, 1897–1901.
62. S. F. Liu, T. Fukuyama, M. Sato and I. Ryu, *Organic Process Research & Development*, 2004, **8**, 477-481.
63. M. T. Rahman, T. Fukuyama, N. Kamata, M. Sato and I. Ryu, *Chemical Communications*, 2006, 2236-2238.
64. G. Shore, S. Morin, D. Mallik and M. G. Organ, *Chemistry-a European Journal*, 2008, **14**, 1351-1356.
65. A. Nagaki, A. Kenmoku, Y. Moriwaki, A. Hayashi and J.-i. Yoshida, *Angewandte Chemie-International Edition*, 2010, **49**, 7543-7547.
66. G. I. Taylor, *Proc. R. Soc. Lond. A*, 1932, **138**, 41-48.
67. R. G. Cox, *Journal of Fluid Mechanics*, 1969, **37**, 601-623.
68. S. Torza, R. G. Cox and S. G. Mason, *Journal of Colloid and Interface Science*, 1972, **38**, 395-411.
69. S. Guido and M. Villone, *Journal of Colloid and Interface Science*, 1999, **209**, 247-250.
70. R. B. Bird, W. E. Stewart and E. N. Lightfoot, *Transport Phenomena*, Wiley, 2007.
71. G. Hetsroni, S. Haber and E. Wacholder, *Journal of Fluid Mechanics*, 1970, **41**, 689-705.
72. B. P. Ho and L. G. Leal, *Journal of Fluid Mechanics*, 1975, **71**, 361-383.

73. M. J. Martinez and K. S. Udell, *Journal of Fluid Mechanics*, 1990, **210**, 565-591.
74. C. Richards, G. J. T. Tiddy and S. Casey, *Langmuir*, 2007, **23**, 467-474.
75. J. A. Stewart, A. Saiani, A. Bayly and G. J. T. Tiddy, *Colloids and Surfaces A: Physicochemical and Engineering Aspects*, 2009, **338**, 155-161.
76. S. Caserta, M. Simeone and S. Guido, *Physical Review Letters*, 2008, **100**, 137801.
77. V. Sibillo, G. Pasquariello, M. Simeone, V. Cristini and S. Guido, *Physical Review Letters*, 2006, **97**, 054502.
78. J. L. Berna, C. Bengoechea, A. Moreno and R. S. Rounds, *Journal of Surfactants and Detergents*, 2000, **3**, 353-359.
79. P. G. De Gennes, *The Physics of Liquid Crystals*, New York, 1974.
80. S. Caserta, S. Reynaud, M. Simeone and S. Guido, *Journal of Rheology*, 2007, **51**, 761-774.
81. J. Deschamps, V. Kantsler and V. Steinberg, *Physical Review Letters*, 2009, **102**, 118105.
82. G. Platz and C. Thunig, *Langmuir*, 1996, **12**, 1906-1912.
83. C. S. Rosenblatt, R. Pindak, N. A. Clark and R. B. Meyer, *Le Journal De Physique*, 1977, **38**, 1105-1115.
84. C. Blanc and M. Kléman, *The European Physical Journal B - Condensed Matter and Complex Systems*, 1999, **10**, 53-60.

85. G. K. Auernhammer, H. R. Brand and H. Pleiner, *Rheologica Acta*, 2000, **39**, 215-222.
86. G. K. Auernhammer, H. R. Brand and H. Pleiner, *Physical Review E*, 2002, **66**, 061707.
87. S. Chatterjee and S. L. Anna, *Physical Review E*, 2012, **85**, 011701.
88. S. Guido and F. Greco, *Rheology Reviews*, 2004, 99-142.
89. F. Nallet, D. Roux and J. Prost, *Physical Review Letters*, 1989, **62**, 276-279.
90. A. W. Holland, *Demystifying Microwave Assistance in Homogeneous Catalysis: Chemical Kinetics of Microwave-Heated Palladium Reactions* in: A.C.S.P.R. Fund (Ed.), 56th Annual Report on Research 2011.

8. Appendix

8.1. Publications

1. **A. Pommella**, S. Caserta, V. Guida, S. Guido “Shear-Induced Deformation of Surfactant Multilamellar Vesicles”, *Physical Review Letters* 108, 138301 (2012),
doi: <http://link.aps.org/doi/10.1103/PhysRevLett.108.138301>;
2. **A. Pommella**, G. Tomaiuolo, A. Chartoire, S. Caserta, G. Toscano, S. P. Nolan, S. Guido “Palladium-N-heterocyclic carbene (NHC) catalysed C-N bond formation in a continuous flow microreactor. Effect of process parameters and comparison with batch operation.”, *Chemical Engineering Journal* (2013),
doi: <http://dx.doi.org/10.1016/j.cej.2013.03.070>;
3. **A. Pommella**, S. Caserta, S. Guido “Dynamic flow behaviour of surfactant vesicles under shear flow. Role of multilamellar microstructure”, *Soft Matter* (submitted);
4. **A. Pommella**, V. Preziosi, S. Caserta, J. M. Cooper, S. Guido, M. Tassieri “Rheological characterization of very low viscoelastic polyelectrolytes solutions: a comparison between optical tweezers and bulk rheometry”, *Langmuir* (in preparation).

8.2. Conferences

1. **A. Pommella**, S. Caserta, V. Guida, S. Guido "*Deformazione di vescicole di surfattante in flusso di shear mediante tecniche di video-microscopia ottica*" Convegno GRICU 2012 16-19 September 2012, Montesilvano (Italy);
2. **A. Pommella**, G. Tomaiuolo, S. Caserta, S. Guido "*Confronto tra batch e microreattori a flusso continuo per sintesi C-N cross-coupling*" Convegno GRICU 2012 16-19 September 2012, Montesilvano (Italy);
3. V. Preziosi, **A. Pommella**, G. Tomaiuolo, S. Caserta, S. Guido "*Analisi della deformabilità di una singola goccia in un flusso alla Poiseuille*" Convegno GRICU 2012 16-19 September 2012, Montesilvano (Italy);
4. **A. Pommella**, S. Caserta, V. Guida, S. Guido "*Deformation of multilamellar surfactant vesicles under shear flow*" The XVth International Congress on Rheology 5-10 August 2012, Lisbon (Portugal);
5. S. Guido, S. Caserta, V. Preziosi, **A. Pommella** "*Mixing efficiency of low viscosity Boger fluids*" The XVIth International Congress on Rheology 5-10 August 2012, Lisbon (Portugal);
6. G. Tomaiuolo, V. Preziosi, **A. Pommella**, S. Caserta, S. Guido "*Motion and deformation of droplets in micro-confined capillary*

- flow*" The XVIth International Congress on Rheology 5-10 August 2012, Lisbon (Portugal);
7. **A. Pommella**, S. Caserta, V. Guida, S. Guido "*Flow induced deformation of multilamellar surfactant vesicles*" XII Convegno Nazionale della Società Italiana di Reologia 3-6 July 2012, Ustica (Italy). ISBN: 978-88-904912-2-1;
 8. V. Preziosi, **A. Pommella**, G. Tomaiuolo, S. Caserta, S. Guido "*Flusso Confinato in Microcapillari di Miscele Bifasiche Liquido-Liquido*" XII Convegno Nazionale della Società Italiana di Reologia 3-6 July 2012, Ustica (Italy). ISBN: 978-88-904912-2-1;
 9. **A. Pommella**, S. Caserta, V. Guida, S. Guido "*Reo-Optical investigation of shear induced deformation of multilamellar surfactant vesicles*" 5th International Workshop Bubble and Drop Interfaces 20-24 May 2012, Krakow (Poland). ISBN: 978-83-60514-16-0;
 10. S. Caserta, V. Preziosi, **A. Pommella**, S. Guido "*Mixing of Liquid-Liquid Non-Newtonian Fluids, Preliminary Results.*" 12th International Conference Multiphase Flow in Industrial Plants 21-23 September 2011, Napoli (Italy). ISBN: 978-88-89677-22-3;
 11. **A. Pommella**, S. Guido "*Flow chemistry in catalytic microreactors. Applications to Buchwald-Hartwig amination*" Synflow Meeting 7 June 2011, St Andrews (Scotland);

12. **A. Pommella**, S. Caserta, V. Guida, S. Guido "*Deformazione di vescicole di surfattante in flusso di shear*" XI Convegno Nazionale della Società Italiana di Reologia 23-26 May 2010, Trieste (Italy);
13. **A. Pommella**, S. Caserta, S. Guido "*Shear – induced deformation of HLAS vesicles*" 6th Annual European Rheology Conference 7-9 April 2010, Goteborg (Sweden).